Bimodal AFM Using State Estimation and In Vitro AFM Imaging of Microtubules

A THESIS
SUBMITTED TO THE FACULTY OF THE GRADUATE SCHOOL
OF THE UNIVERSITY OF MINNESOTA
BY

Carmen Li

IN PARTIAL FULFILLMENT OF THE REQUIREMENTS
FOR THE DEGREE OF
MASTER OF SCIENCE IN ELECTRICAL ENGINEERING

Advisor: Professor Murti V. Salapaka

December, 2015

Acknowledgements

I would like to acknowledge the following individuals for their contributions to my thesis and research:

- My advisor, Professor Murti Salapaka, for his guidance and support throughout my research experience

- Dr. Greg Haugstad and Professor Andrew Lamperski for willing to serve on my committee and to provide useful feedback. I want to acknowledge Dr. Haugstad for providing insightful discussions on AFM and polymer sample for my work

- Professor Melissa Gardner's group for providing microtubules samples

- All of my colleagues in the Nano Dynamics Systems group during the 2012-2015 year who have provided me assistance and feedback

I would also like to thank my family and friends for their encouragement and Vlad for his unwavering support and belief in me.

Abstract

Advancement in atomic force microscope (AFM) techniques such as bimodal and multifrequency AFM modes provide new ways to discern material property contrast with greater resolution and specificity at the micro- and nano-scales. However, most AFM techniques to date demodulate the cantilever's deflection signal at each eigenmode's resonance frequency to infer tip-sample interactions. This approach neglects each mode's entire contribution, which includes frequency contents away from the modal resonance frequency, and leaves out potentially useful signals. Furthermore, the need to quantify the energy of the individual eigenmode becomes important when there is energy transfer between eigenmodes, as in the case of a soft cantilever in liquid. This thesis uses a receding horizon Kalman filter to decouple the eigenmodes prior to quantifying the average power of the individual mode in the bimodal experiments in air and liquid. It further shows that capturing the average power of the PLMA-PBMA polymer domains from frequencies away from resonance provides a tool to discern the different polymer domains when the input energy level of the two eigenmodes is approximately equal. Finally, a microtubules imaging in buffer protocol that could be used in multifrequency imaging application is presented.

Table of Contents

List of Tables

List of Figures

Chapter 1: Introduction

Since its invention [1] the Atomic force microscope (AFM) has been an indispensable tool in nanotechnology and basic science research due to its ability to interrogate materials with sub-nanometer resolution. AFM has been widely used to study physics and biochemistry phenomena such as the assembly and disassembly of microtubules, surface chemistry, polymer phase separation, and protein formation with forces in the nano- and pico-newton ranges. AFM has advanced from static force and topography imaging to techniques that could deduce material properties with greater resolution and bandwidth [2]. The earliest AFM application is the constant force mode or contact mode. The sharp tip at the end of a cantilever ranging in tens of micrometers scans over the sample surface, and as the cantilever bends the laser spot reflecting off the back of the cantilever onto a position sensitive photodiode detector is used as a continuous force feedback signal. Even though contact mode AFM provides a straight forward force interpretation using Hook's law, the drawback is that the tip exerts large lateral force on the sample and creates wears on the tip and the sample. Being an intermittent contact mode, the dynamic AFM is more suitable for imaging soft samples such as polymer and biological samples by minimizing lateral forces; however its dynamics and interpretation of data are more complex. In dynamic AFM the cantilever is driven by a piezo dither near its fundamental frequency at constant amplitude as shown in Figure 1.1. The piezo scanner adjusts the vertical position of the tip or sample to maintain constant cantilever amplitude as the tip raster-scans the sample. A lock-in amplifier is used to extract the cantilever amplitude and phase lag relative to the drive signal to reconstruct sample topography and deduce material properties. The oscillating tip probes the distance-dependent forces as it taps the sample during each oscillation cycle. These distance-dependent attractive and repulsive forces perturb the tip oscillation and cause the cantilever to bend. Understanding the measured bending dynamics allow quantitative study of material properties.

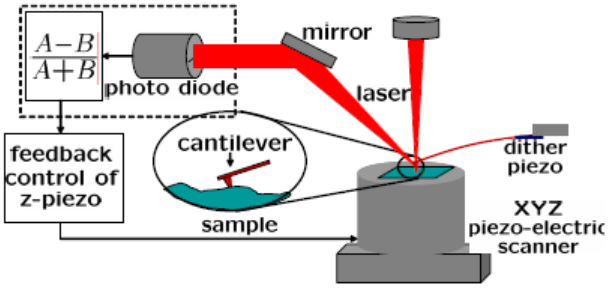

Figure 1.1: Conventional Dynamic AFM operation **[2]**

There is a wealth of literature on the study of dynamic AFM using a single eigenmode cantilever theory. The oscillating cantilever is often described as spring-mass-damper system, and this single mode approach is often sufficient to explain many dynamic AFM phenomena such as physical hysteresis (i.e. jump-to-contact and jump-from-contact) during force curves and the bi-stable attractive and repulsive imaging regimes [3]. The system perspective of dynamic AFM has further contributed to the explanation of the sinusoidal nature of the tip trajectory using harmonic balance principles [4], the development of observer-based high bandwidth transient-signal AFM [5], and the real time imaging of conservative and dissipative forces of polymer samples [6].

1.1 Higher Frequency AFM

It is well accepted that the nonlinear tip-sample interaction forces excite higher harmonics of the tip oscillation [7], and that there is a coupling of energy to higher eigenmode in the repulsive tip-sample interaction [8]. There has been significant interest in recent years to exploit these higher harmonics and higher-frequency signals. Higher frequencies and multifrquency dynamic AFM techniques [9] have provided enhanced material contrast through excitation of higher cantilever eigenmodes and harmonics. These higher frequency contents could be generated indirectly through nonlinear tip-sample interactions or by direct higher frequency forcing. For instance, in bimodal AFM mode the cantilever is forced at two eigenmode resonant frequencies and lock-in amplifiers are used to track the amplitude and phase of each eigenmode resonant frequency, as shown in Figure 1.2. Detection of higher frequencies requires a broadband instrumentation. Multiple digital lock-in amplifiers are needed to track the amplitude and phase at each frequency in addition to the intermodulation products.

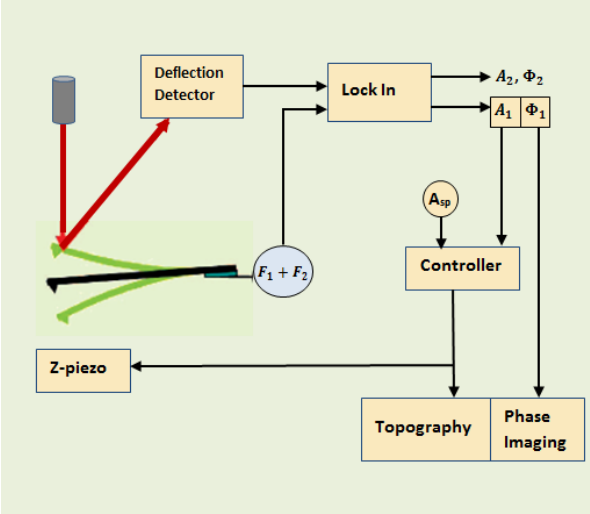

Figure 1.2: In the typical bimodal dynamic AFM operation, two external excitation signals, $\boldsymbol{F_1}$ and $\boldsymbol{F_2}$, are added to drive the cantilever. The excitation signal is chosen near the resonant frequency of the first and second mode. This signal is fed back to the lock-in amplifiers, and the first and second mode signals are demodulated at the drive frequencies to obtain the amplitude and phase signals for each mode. The first mode amplitude signal is used as the feedback to the Z-peizo, whereas the second mode is exploited to obtain additional material property contrast. $\boldsymbol{A_{sp}}$ is the amplitude setpoint imaging parameter.

Furthermore, recent studies have shown that in dynamic mode AFM in liquid, the single mode approach is not sufficient to capture the cantilever dynamics where multiple modes participate in a significant manner. Basak et. al. [10] shows that for soft cantilever in liquid there is momentary excitation of the second eigenmode as the tip interacts with the sample even though only the fundamental resonant frequency is excited. This bimodal phenomenon has been attributed to the three-fold decrease in the cantilever's quality factors by hydrodynamic damping. Melcher et. al. [11] found that the phase contrast in liquid imaging of low stiffness cantilever probes derives primarily from a unique energy flow channel from the momentary excitation of higher eigenmodes, and that the phase information is the map of short-range conservative interactions rather than the tip-sample dissipation. Therefore, using only a single mode approximation to characterize the cantilever dynamics in liquid could lead to inaccurate interpretation of material properties since phase imaging is based on the assumption that the single eigenmode fully captures the cantilever dynamics.

1.2 Motivation and Scope

There is a need to quantify the contribution of higher eigenmodes in dynamic AFM for accurate interpretation of material contrast in experimental data. Lock-in amplifier is widely used to extract the modal information at each mode's resonant frequency, and the resulting amplitude and phase are used to quantify the contribution of each mode. Saraswat et. al. [12] reasons that the effect or energy of a higher eigenmode cannot be fully captured using lock-in demodulation since the contribution of a mode may be present away from the modal resonant frequency. Furthermore, the steady-state amplitude and phase signals in the lock-in method are slow varying and might not be able to capture transient signals such as the momentary excitation of higher eigenmodes. Saraswat et. al. [12] developed a receding horizon Kalman filter observer-based state-detection scheme that has the capability of tracking effects away from the modal frequency and to detect the higher mode participation in air.

Current research on higher eigenmode enhancement in air and liquid are typically simulated and analyzed using physics based modeling of the cantilever [13] . Multi-mode analysis of the cantilever dynamics relies on accurate modeling of intermolecular forces at the solid-solid and liquid-solid interfaces. These complex dynamics present a challenge in the physics modeling approach. On the other hand, the study of higher eigenmode influences from a system perspective allows the quantification of the contribution of the higher eigenmodes even when the physics model is incomplete, as long as the dynamical model of the cantilever system is experimentally obtained from frequency-sweep method. Systems approach allows the optimal estimation using Kalman filtering to estimate the cantilever deflection of an individual eigenmode. This thesis looks at the overall effect of the second mode during tip-sample interaction and quantifies the individual eigenmode contribution in bimodal AFM in air and in liquid using state estimation. This thesis further investigates the effects that changing the energy input ratio of the first and second eigenmodes have on discerning the different polybutyl methacrylate (PBMA) and polylauryl methacrylate (PLMA) domains. The algorithm in [12] is adapted to analyze the data in both air and liquid applications.

The usefulness of the AFM in biological research lies in its ability to image biological samples in their near native physiological environment, which is usually buffer. One of the challenges of AFM in biology imaging is the chemistry of sample preparation. The second objective of this thesis is to provide a protocol for microtubules imaging under buffer, which

allows future analysis of material properties in liquid using techniques developed in the Nano Dynamics Systems group.

1.2.1 Organization of Thesis

Chapter 2 provides the background information on the multimode cantilever dynamics, tip-interaction forces, receding horizon Kalman filter, and solenoid-based magnetic actuator construction. Chapter 3 describes the experimental setup, frequency response collection, magnetic actuation circuitry, and methodology. Chapter 4 presents the results of the bimodal experiments in air for mica and PLMA-PBMA samples. Chapter 5 presents the results of AFM experiments conducted in liquid. Chapter 6 presents the microtubules protocol and imaging in buffer. Conclusion of the work is given at the end.

Chapter 2: Background

2.1 Cantilever Dynamics

The perturbed bending of the cantilever when the tip intermittently taps on the sample contains the tip-sample forces and material properties information. Understanding the cantilever bending dynamics is crucial to the deduction of the sample's material properties. A static analysis of shear forces and bending moment of a volume in a cantilever beam describes the bending of cantilever under static loading. In dynamic AFM the cantilever has both spatial and temporal variation, and the deflection of a cantilever in Figure 2.1 is described by the Euler-Bernoulli partial differential.

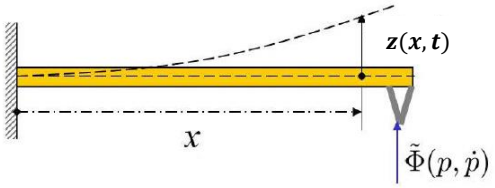

Figure 2.1: Fix-free cantilever beam subjected to a static loading force modeled by tip-sample interaction force $\tilde{\boldsymbol{\Phi}}(\boldsymbol{p},\dot{\boldsymbol{p}})$, where $\boldsymbol{p}$ and $\dot{\boldsymbol{p}}$ are the cantilever tip position and velocity, respectively **[14]**.

Treating the cantilever as an elastic beam with one end fixed *(x=0)* and the other end free (*x=L*), the undamped free vibration of the cantilever [14] is described by

$$EI\frac{\partial^4 z(x,t)}{\partial x^4} + \rho A\frac{\partial^2 z(x,t)}{\partial t^2} = 0. \tag{1}$$

This is a 4th order partial differential equation. Consequently, four boundary conditions are required and are as follows:

$$z(0,t) = 0, \qquad \frac{\partial z(0,t)}{\partial x} = 0, \tag{2}$$

$$EI\frac{\partial^2 z(L,t)}{\partial^2 x} = 0\,, \;\; EI\frac{\partial^3 z(L,t)}{\partial^3 x} = 0,$$

where $z(x,t)$ is the cantilever displacement at spatial coordinate x and time t, E is the Young's modulus, I is the moment of inertia, ρ is the density, and A is the cross section area. In dynamic AFM the tip interacts with sample intermittently, therefore the mode shapes are mostly dictated

by the fixed-free conditions [14] [15] . The *N* mode solution to the beam equation is of the form $z(x,t) = \sum_{j=1}^{N} \psi_j(x) q_j(t)$, where ψ_j(x) is the j^{th} mode deformation, and $q_j(t)$ satisfies

$$\frac{\ddot{q_j}}{\omega_j^2} + \frac{\dot{q_j}}{\omega_j Q_j} + q_j = \frac{g_j(t)+\eta_j(t)}{k_j} + \frac{\Phi_j(p,\dot{p})}{k_j}. \quad (3)$$

Let $g_j(t) = \psi_j(L) g(t)$ be the external sinusoidal excitation to the cantilever and $\Phi_j(p,\dot{p}) = \psi_j(L)\Phi(p,\dot{p})$ be the sample interaction forcing at $x = L$, and $p(t) := z(L,t)$. Using variational principles [15] the displacement of the forced cantilever by a time varying force can be rewritten as a weighted combination of the fundamental mode deformation of the unforced cantilever. The j^{th} mode thermal noise forcing, resonant frequency, spring constant, and quality factor are $\eta_j(t)$, ω_j, k_j and Q_j, respectively. The dimensionless quality factor indicates the resonating cantilever's energy loss to the environment, and higher Q systems lose energy more rapidly at frequency away from its resonance than lower Q systems.

2.1.1 First Mode Approximation

The cantilever in the conventional dynamic mode AFM is excited at or near its fundamental resonant frequency. Even though a cantilever is a continuous structure, modeling the cantilever as a spring-mass-damper system with a single degree of freedom is widely used and accepted when imaged in air or vacuum environment due to the high quality factor of the cantilever [16]. In air the point mass model is valid, and a good approximation of the tip-cantilever is that of a shaken beam with stiffness and effective point mass attached to a spring [17].

High quality factor cantilevers are used to maximize imaging resolution. The conventional dynamic mode AFM uses steady state signal of the cantilever as the feedback signal. Consequently, even though a high Q cantilever enhances image resolution, it has a longer steady state settling time and limits the detection and imaging bandwidth. Using the steady state part of the cantilever dynamics to image samples means that transient signals, such as the enhancement of higher eigenmodes, are not typically observed. This trade-off in resolution and bandwidth in dynamic mode AFM is overcome by the transient-signal-based method reported in [5] and [18], where the second mode participation in the typical dynamic mode operation is observed. The effect of the second mode shows up as high frequency contents in the innovation signal, or output prediction error, after an initial change in the cantilever dynamics. This methodology utilizes a Kalman observer to exploit the transient part of the cantilever dynamics to

interrogate materials at high bandwidth independent of the quality factor. The construction of the Kalman observer is described in Section 2.3.

In the absence of tip-sample interaction, the deflection of the cantilever forced by external sinusoidal force $g(t)$ and thermal noise is rewritten as

$$\ddot{q}_j(t) + \frac{\omega_j}{Q_j}\dot{q}_j(t) + \omega_j^2 q_j(t) = \frac{1}{m}\,(\eta(t) + g(t)). \tag{4}$$

In the Laplace domain the transfer function G(s) is described by the second order system with a right half plane zero [19],

$$G(s) = \frac{\frac{k}{m(c_1+c_2 s)}}{s^2+\frac{\omega_0}{Q}s+\omega_0^2}\,. \tag{5}$$

The above cantilever transfer function corresponds to the point mass description by choosing $c_1 = 1$ and $c_2 = 0$. In a two mode analysis, the above second order transfer function is added in the linear approximation. The parameters of the second mode transfer function can be obtained experimentally. The single mode oscillator forms the basis for phase imaging for material properties interrogation under ambient and vacuum conditions [20]. The phase shift of the tip with respect to the drive signal is mapped over the sample, where the tip-sample dissipation is the difference between the work input to the oscillator and energy lost to the surrounding.

2.1.2 Tip-Sample Interaction Forces

For the nonlinear tip-sample interaction forces, the dominant forces in air are different than in liquid due to the different nanoscale forces at the liquid-solid interface and the low quality factors [13]. In air the cantilever tip encounters attractive van der Waals attractive force and short range repulsive force as the cantilever taps on the sample. The tip traverses a large deflection as described by the nonlinear interaction force vs. distance Lennard-Jones models [2]. Material properties can be inferred from the bending as the tip experiences long range attractive forces and short range repulsive forces through each oscillation cycle. Various continuum elasticity theories are used to describe the short range contact and adhesion between the tip and sample. The Hertz contact model is a simple case of elastic deformation of two homogenous spheres under external load. The Johnson-Kendall-Roberts (JKR) and Derjaguin-Muller-Toporov (DMT) models modify the Hertz model by taking adhesion force into the analytical description of the deformation [17].

In liquid the attractive region is mostly electrostatic in nature. In air, the capillary force due to the water vapor at the sample surface is prevalent; the capillary force is negligible in liquid. In liquid the rectangular cantilever is subject to a hydrodynamic damping force, a driving force, and a tip-sample interaction force [13]. The large hydrodynamic drag in liquid decreases the quality factors of the cantilever resonance by at least three-fold. Therefore, the analysis techniques used for high Q cantilever resonance are not as applicable to liquid application.

2.2 Systems Perspective

From the systems perspective, the input to the AFM is the excitation signal to the piezoelectric shake or magnetic actuator, and the output is the photodiode detector voltage representing the cantilever deflection. The tip-sample dynamics is complex and highly nonlinear. In Figure 2.2 the nonlinear tip-sample interaction forces are represented by ϕ that is in feedback with the LTI cantilever system G. Formulating the tip-sample interaction as an output feedback to a LTI cantilever system with equivalent stiffness and damping allows the construction of a recursive estimation of equivalent parameters (REEP) algorithm to study material properties [21]. The REEP algorithm was implemented on a FPGA platform to interface with a commercial AFM to provide real time imaging of the conservative and dissipative forces [6].

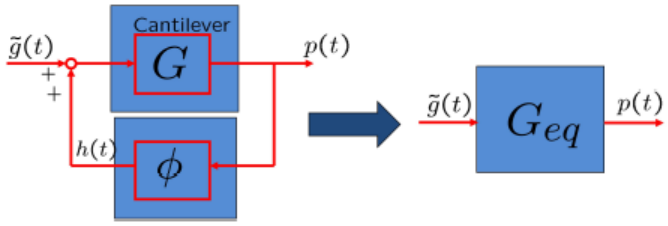

Figure 2.2: Equivalent cantilever system **[14]**

2.2.1 State Space Model

The state space model of a forced oscillatory cantilever in dynamic AFM is obtained from the experimental transfer function. The cantilever system is modeled as a linear and time invariant system. Consider a linear plant with the following state space representation with process noise w and measurement noise v:

$$\dot{x} = Ax + B(u + \eta), \tag{6}$$
$$y = Cx + v.$$

The A matrix relates the past states to the current states of the dynamical system. The B matrix links the states to the input, or external force applied to the cantilever. The observation matrix C links the measurement to the states, and D is the feedforward matrix. The state vector x contains the cantilever position and velocity, u is the external input, and y is the measured cantilever deflection from the photodiode detector. The process noise η and measurement noise v are zero mean Gaussian processes independent from each other. The state space representation of the Equation (3) is described by

$$\begin{bmatrix}\dot{x}_{1j}\\ \dot{x}_{2j}\end{bmatrix} = \begin{bmatrix}0 & 1\\ -\omega_j^2 & \frac{-\omega_j}{Q_j}\end{bmatrix}\begin{bmatrix}x_{1j}\\ x_{2j}\end{bmatrix} + \begin{bmatrix}0\\ \frac{\omega_j^2}{k_j}\end{bmatrix}\left(f_j + \eta_j\right), \tag{7}$$

$$y_j = \varphi_j(L)[1 \quad 0]\begin{bmatrix}x_{1j}\\ x_{2j}\end{bmatrix},$$

where $y_j = \psi_j(L)q_j$ is the contribution of the j^{th} mode to the cantilever tip deflection p, $p = \sum_{j=1}^{N} y_j$, and $f_j := \psi_j(L)(g(t) + \Phi(p,\dot{p}))$. Let $B_j^L = B_j\psi_j(L)$, then Equation (7) can be written as

$$\dot{x}_j = A_j x_j + B_j^L\left(g(t) + \Phi(p,\dot{p})\right) + B_j\eta_j\,, \tag{8}$$

$$y_j = C_j x_j,$$

with the state vector $x_j = [x_{1j}\ x_{2j}]'$. The discretized model is

$$x_j(k+1) = F_j x_j(k) + G_j^L\left(g(k) + \Phi(p,\dot{p})\right) + G_j\eta_j(k), \tag{9}$$

$$y_j(k) = H_j x_j(k),$$

for $j = 1, 2, \ldots N$, $x(k) = [x_1(k) \quad x_2(k) \quad \ldots \quad x_N(k)]'$. Equation (7) for each mode can be combined as a linear superposition to the following

$$x(k+1) = \begin{bmatrix}F1 & \ldots & 0\\ 0 & \ddots & 0\\ 0 & 0 & F_N\end{bmatrix}x(k) + \begin{bmatrix}G_1^L\\ \vdots\\ G_N^L\end{bmatrix}\left(g(k) + \Phi(p,\dot{p})\right) + \begin{bmatrix}G_1 & \ldots & 0\\ 0 & \ddots & 0\\ 0 & 0 & G_N\end{bmatrix}\begin{bmatrix}\eta_1(k)\\ \vdots\\ \eta_N(k)\end{bmatrix}, \tag{10}$$

$$y(k) = [H_1 \quad \ldots \quad H_N]x(k) + v(k).$$

All the $\eta_j's$ are independent and Gaussian with the covariance matrix $E(\eta\eta^*) = S$. The multi-mode model for the cantilever described in Equation (10) was used to study the first and second flexure eigenmodes of a cantilever.

2.3 Parameter Estimation using Kalman Filter

Modeling the cantilever system as a state space system allows state estimation using Kalman filtering to estimate the contribution of the second eigenmode. The Kalman filter has wide application in engineering in linear systems ranging from aerospace to chemical refinery processes. The Kalman filter provides estimation and prediction of the states of a dynamical system given the mathematical model of the dynamical system and updated measurements. It provides the optimal solution in the minimization of the mean square errors of $x_k - \hat{x}_k$, where $\hat{x}_k$ is the estimate of the state x_k that we wish to estimate based on the available measurements. The filter uses a priori information for prediction and a posteriori information to update the estimation once a measurement is available. An extended Kalman filter for nonlinear system is linearized about the equilibrium point. Since it is a recursive filter, there is no need to store past measurements in computing the present estimate. Observer-based AFM applications using Kalman filtering have been successfully used to detect transient signals [5] [22] with high bandwidth and provide real-time measures on AFM image reliability [23] through the innovation signal, which is the error of the estimated observation from the actual measurement. The discrete Kalman filter could be derived by optimizing the assumed form of the linear estimator, and the derivation is shown in [24]. The discrete time Kalman observer model is

$$\hat{x}_{k+1} = F\hat{x}_k + G^L g_k + L_k(y_k - H\hat{x}_k), \tag{11}$$
$$\hat{y}_k = H\hat{x}_k,$$

where L_k is the Kalman filter gain. The Kalman filter schematic as applied to AFM systems is given in Figure 2.3.

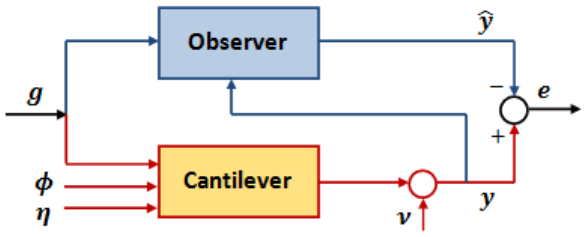

Figure 2.3: Observer-based AFM system. The observer mimics the dynamics of the cantilever and provides the estimate the cantilever state. The error $\boldsymbol{e}$, or the innovation signal, is the difference between the actual output $\boldsymbol{y}$ and estimated output $\hat{\boldsymbol{y}}$. The dither input to the observer and cantilever system is denoted by $\boldsymbol{g}$. The tip-sample interaction force, process noise, and measurement noise, are denoted by $\boldsymbol{\phi}$, $\boldsymbol{\eta}$, and $\boldsymbol{\nu}$, respectively. In the AFM system, the process noise and measurement noise come from the thermal noise and photodiode detector noise, respectively **[18].**

2.3.1 Discrete Kalman Filter

A Kalman filter that provides an estimate $\hat{x}_{k+1}$ of the state x of the cantilever, depending on all the observations until time step k, is described by

$$\hat{x}_{k+1} = F\hat{x}_k + FP_kH^T(HP_kH^T + R)^{-1}[y_k - \hat{y}_k] + G^L g_k \,, \tag{12}$$
$$\hat{y}_k = H\hat{x}_k \,,$$
$$P_{k+1} = F[I - P_kH^T(HP_kH^T + R)^{-1}H]P_kF^T + GSG^T.$$

The initial state estimate $\hat{x}$ is set to zero, and the error covariance $P_k = Cov(x_k - \hat{x}_k)$ is initialized by a large number. For computation the discrete Kalman filter has time update equations and measurement update equations [25]. The time update equations are described by the equations in (13).

$$\hat{x}_k = F\hat{x}_{k-1} + G^l g_{k-1} \,, \tag{13}$$
$$P_k^- = FP_{k-1}F^T + S \,.$$

The measurement update equations are described by (14):

$$L_k = P_k^- H^T(HP_k^- H^T + R)^{-1}, \tag{14}$$
$$\hat{x}_k = \hat{x}_k^- + L_k(y_k - H\hat{x}_k^-) \,,$$
$$P_k = (I - L_kH)P_k^- .$$

The time update equations project the state and covariance estimate forward in time. The measurement update computes the Kalman gain L_k for the a posteriori state estimate using the available measurement at step k. Subsequently, the a posteriori error covariance estimate is computed in the above equation.

2.3.2 Receding Horizon Kalman Filter

When the horizon initial state is unknown, as in the initial position of the cantilever, a receding horizon Kalman (RHK) filter can be used to estimate the states of the cantilever [12]. The receding horizon Kalman filter combines the receding horizon strategy with the standard Kalman filter [26]. The RHK filter uses finite measurements and combines the finite impulse response (FIR) filter form to estimate the states for discrete LTI systems. Unlike the steady state Kalman filter that uses the all past measurements to estimate the state variable, the RHK filter

only uses measurements up to the most recent time-horizon. This ensures that dynamics in the past do not heavily influence the current dynamics. The change in tip-sample interaction changes with topography and material properties and may have undue influences on the filter convergence [12]. Thus the RHK filter is a more robust filter. For systems that encounters changing environment, such as the AFM tip as it travels on the terrains of a sample, the receding horizon Kalman filter provides a faster detection that converges since it is not keeping all the state history from the initial time.

2.4 Liquid Magnetic Actuation

In dynamic AFM the forcing signal can be an acoustic, magnetic, or electrical source. The most common way to actuate a cantilever is through acoustic actuation using a piezoelectric element to shake the base of the cantilever holder and drive the cantilever oscillation at or near its fundamental frequency. In air or vacuum, the high quality factor of the cantilever effectively attenuates the piezo shake's resonances, which have quality factors an order of magnitude smaller as compared to the cantilever [27]. As a result, the piezo shake dynamics are not visible in the acoustic frequency sweep data. However, this technique is not suitable for liquid imaging since a cantilever submerged in liquid actuated by a piezo shake yields a complicated, 'forest of peak' resonance response [17]. This is due to the vibration transferred from the piezo to the cantilever through structural-borne and fluid-borne vibration and mechanical excitation of the surrounded water medium [28]. In liquid, the cantilever resonance becomes significantly wider and is unable to filter out the surrounding peaks. To circumvent this challenge, research groups have used solenoid-based actuation of magnetically coated cantilevers [29] [30]. Magnetically actuating a cantilever with a varying magnetic field yields a simpler cantilever response in liquid. Kegashima et. al. [31] has developed a wide-band magnetic cantilever excitation system to study soft matter dynamics. Commercial AFM manufacturers such as Agilent and Asylum Research have developed proprietary magnetic actuation systems.

In magnetic actuation the magnetized cantilever is directly excited by an external magnetic field. The electromagnetic actuator is a solenoid consisting of multiple turns of a wire around a ferrite core. The solenoid exerts a time-varying force on the magnetic cantilever when an alternative current $i(t)$ passes through it. The force F and torque τ exerted on a magnetic dipole m in the presence of a magnetic field B is given by $F = \nabla(Bm)$ and $\tau = B \times m$, respectively [31]. Cantilever deflection is caused by a combination of force and torque. The

magnetic field strength is proportional to the current passing through the solenoid. However, increasing current also increases the solenoid inductance, L. The diameter of the electromagnet must be as small as possible to minimize inductance of the load when driven at high frequency. A, l, μ, and N in Equation (15) correspond to the solenoid's cross section area, length, permeability of the ferrite (manganese zinc), and the number of the turns of wire, respectively.

$$L = \frac{\mu N^2 A}{l} \tag{15}$$

Chapter 3: Methods

3.1 Experimental - Bimodal Excitation in Air

In the bimodal experiments in air, the cantilever is simultaneously driven at its first and second flexure modes' resonance frequency. The HP 4395A network analyzer generates an internal signal and uses the linear frequency sweep method to capture the frequency response of the cantilever system. The two drive signals were generated from the network analyzer and the HP 33120A function generator and were added in an external noninverting summing circuit as shown in Figure 3.1 prior to being routed to the MFP-3D AFM system. The drive frequencies were selected to be at the resonance frequency of the first and second modes. The operational amplifier used in the summing circuit is a wide bandwidth LF351N model. The resistors were chosen such that the output voltage is the sum of the two input signals.

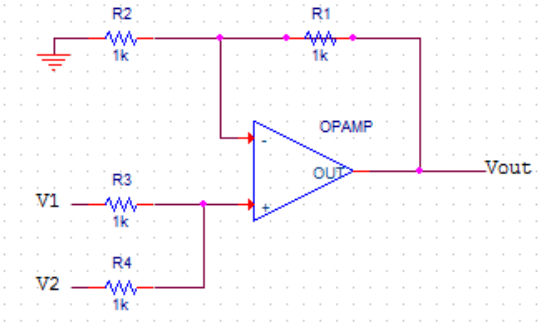

Figure 3.1: Summing operation amplifier circuit

The photodiode detector signal measures the cantilever oscillation amplitude. The cantilever deflection is determined by multiplying the inverse optical lever sensitivity with the measured voltage from the photodiode detector. Each mode's inverse optical lever sensitivity was determined by the static contact force curve on freshly cleaved mica. The cantilever spring constant for each mode was determined from the thermal fluctuation method in the AFM software. The samples consisted of a muscovite mica and spin-coated polybutyl methacrylate (PBMA) and polylauryl methacrylate (PLMA) sample. The mica sample was purchased from Ted Pella. inc. The PLMA-PBMA sample was provided by CharFac at the University of Minnesota. The PLMA-PBMA sample was chosen to obtain a high phase contrast signal. At room temperature the sample is readily phase segregated into three discernible regions: large size PLMA domains, intermediate size PLMA domains, and the PBMA domains.

The goal of the first set of experiments was to obtain a qualitative understanding of the effect of the second mode on material property contrast. Dynamic force curves were collected with cantilever amplitude setpoint at 70% and 75% of the free air amplitude on PLMA-PBMA and mica, respectively. The total drive input to the AFM system produced a 1.1 V amplitude output from the photodiode detector; this corresponded to a cantilever oscillation amplitude of 191.6 nm. The external drive voltage, position sensitive photodiode detector voltage, and the Z sensor voltage were acquired using the National Instruments (NI6341) USB data acquisition module at 2MHz sampling frequency. Buffer circuits were used to condition the signals prior to data acquisition. The results and analysis of this experiment are presented in Chapter 4 section 4.1.

The second set of experiments was carried out using a different AC240TS cantilever to investigate the effect of varying the ratio of the excitation energy of the two modes when the tip was scanning the PLMA-PBMA sample at 62.5% of the tip's free air amplitude. Extensive experiments were carried out by varying the ratio of the energy of the first mode, estimated using, $E_1 = {\omega_1}^2 {A_1}^2$, to the second mode $E_2 = {\omega_2}^2 {A_2}^2$ when the E2:E1 are 0.03:1, 0.2:1, 1:1, 5:1, and 30:1. The first mode's drive amplitude was set at a baseline of 500mv, resulting in an oscillation amplitude of 42.96 nm, while the second mode drive amplitude was adjusted to obtain the desirable energy ratios. A sampling rate of 2.5 MHz was used. During imaging, the MPF-3D's closed-loop XY scanner was used to zoom into the PLMA domains and PBMA domains. Four locations for each domain at each input energy level were captured and analyzed. The result and analysis of this experiment are presented in Chapter 4 Section 4.2.

3.2 Experiment Setup in Liquid

Since biological imaging applications necessitate the use of soft cantilevers, the inherent bimodal characteristic of these low quality factor cantilevers in liquid allows the second mode to be observed even when the cantilever is excited only at its fundamental flexure frequency. The Agilent MAC VIII cantilever used in this experiment had a thin proprietary magnetic coating and a spring constant of 0.32 N/m. The spring constant and inverse optical lever sensitivity were determined using the same procedure described in Section 3.1, except the calibration was performed in water. The solenoid used to magnetically actuate the cantilever is made of a ferrite core with enameled copper wire windings. The ferrite (manganese-zinc) core diameter and length are 1.5mm and 15mm, respectively. The copper wire diameter is 0.15mm, and it is wound around

the ferrite core 40 times. The relative permeability of the core is approximately 200 (dimensionless). Using (16) the inductance of the solenoid is approximately 200uH. Figure 3.2 shows the circuit used to drive the solenoid.

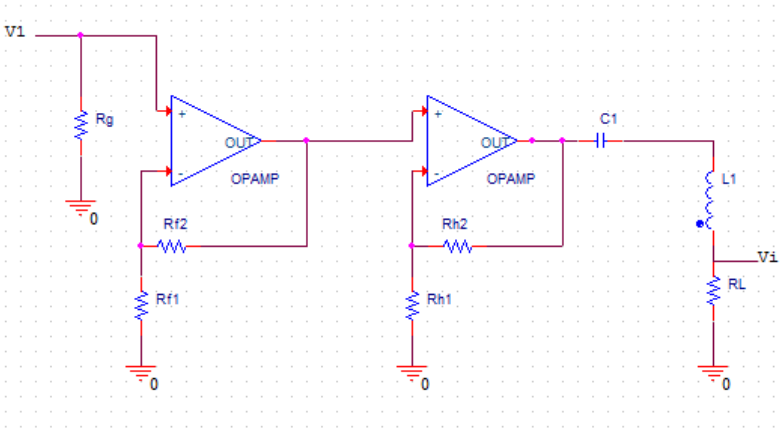

Figure 3.2: Magnetic actuation circuit

A small value R_g resistor in parallel with the input voltage is used to provide a return path to ground for the very small input current. The source signal from the network analyzer was amplified by a LF3571N operational amplifier and a high voltage/current gain operation amplifier (Texas Instruments OP547). The resistor values in the circuit were selected such that the total gain of the circuit is 10, and the output voltage is between ±10 volts. A coupling capacitor was used to by-pass the DC signal and couple only the AC signal to the solenoid. R_L is the sensing resistor with 18 ohms. The current in the circuit was limited to 500mA based on the ampere rating of the copper wire. A Pspice simulation of the circuit was used to verify minimum circuit gain attenuation at the frequency range of interest. The impedance of the solenoid is the sum of the resistance of the copper wire and the solenoid inductance.

The frequency response of the magnetic cantilever immersed in distilled water from 3 KHz to 130 KHz frequency band was captured using the HP 4395A network analyzer. The cantilever tip was positioned far from the mica sample during the frequency sweep to obtain the sample-free cantilever plant. The excitation frequency to the solenoid was near the cantilever's first mode resonant frequency and was identified from the frequency sweep data.

The sample used in this experiment was a mica disc glued to a thin plastic slide. Small magnets were used to hold the plastic slide and solenoid apparatus in place on the MFP-3D AFM stage so that the solenoid could be move to a location where maximum torque was exerted on the

magnetic cantilever. To bring the cantilever under liquid, a droplet of distilled water was placed on mica in sufficient volume such that the tip was fully immersed in the droplet and formed a meniscus between the sample and cantilever holder. A pipette was used to add water to the sample in between imaging operation to maintain the meniscus. The photodiode detector voltage and input signal were captured while the tip was scanning the mica sample at amplitude setpoint of 78%, 65%, and 52% of the free air amplitude. The sinusoidal signal input to the solenoid circuit and photodiode detector voltage were captured using the data acquisition system at 2MHz sampling frequency.

3.3 Computational

The cantilever frequency response obtained from the network analyzer was used to generate a state space model for the individual eigenmode in Matlab. Various fitting functions were used to fit those data to provide the best fit models for the frequency responses. The excitation input signals, cantilever deflection output voltage, and cantilever model were used as input parameters to the receding horizon Kalman filter algorithm to generate a decoupled first mode and second mode deflection data. The root mean square and bandpower functions in Matlab were used to quantify the deflection signals.

3.4 Microtubules Imaging

The goal of this experiment is to provide a sample preparation and imaging protocol for microtubules in buffer using the MFP-3A AFM. The experimental method for microtubules imaging under buffer is discussed in Chapter 6.

Chapter 4: Bimodal Experiment in Air

4.1 Bimodal Imaging of Mica and PLMA-PBMA

The first section of this chapter presents the data and results from the bimodal experiment in air. The experimental frequency responses of the AC-240TS cantilever in air for the first mode and second mode are shown in Figure 4.1. Each of the frequency response data was fitted with a second order simple harmonic oscillator (SHO) with damping. The first order numerator and second order denominator of the transfer function for each mode was obtained using the *invfreqs* function in Matlab. The magnitude of the second mode shows a better SHO fit compared to the first mode, and the second mode phase shift is closer to the predicted 180 degree for a second order system. Three AC-240TS cantilevers had shown similar first mode frequency response. For the second mode, there is a 0.5% difference between the quality factor obtained from the SHO fit and the quality factor determined using the thermal fluctuation method in the AFM software. For the first mode, the quality factor difference is 2.5%. The transfer function of each mode was converted to the state space model describe by Equation (7). The two modes were then combined to form the bimodal cantilever system.

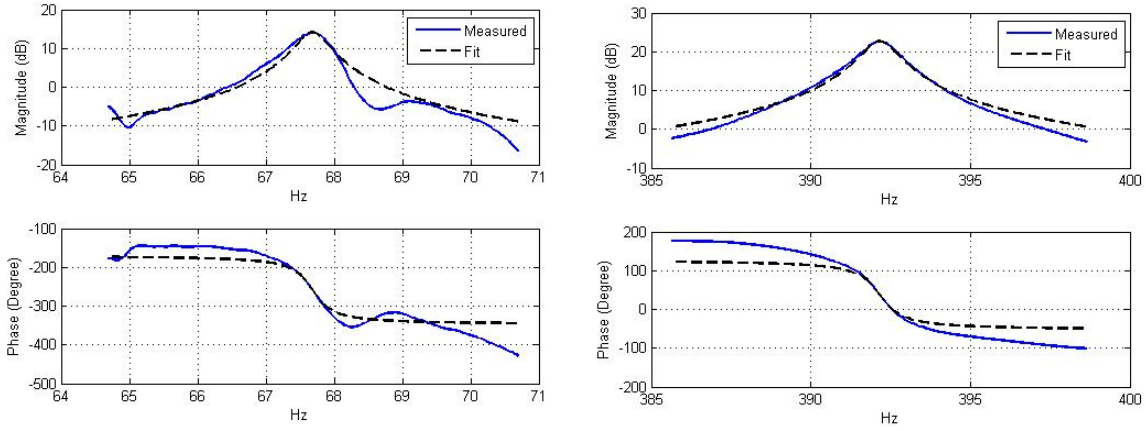

Figure 4.1: SHO Fit for the first mode (left) and second mode (right) frequency response data

The resonant frequency, quality factor, spring constant, and inverse optical lever sensitivity of the first mode and second mode are shown in Table 4.1.

	1st Mode	2nd Mode
Resonant Frequency *f*	66.286 KHz	384.04 KHz
Quality Factor *Q*	129.972	344.958
Inverse Optical Lever Sensitivity	196.1 nm/V	80.78 nm/V
Spring Constant *k*	1.79 N/m	35 N/m

Table 4.1: Modal parameters of the first and second eigenmodes

In bimodal excitation the output from the photodiode detector contains the deflection contributions due to the first mode and second mode. Since the tip-sample interaction forces spread energy from the resonant to the surrounding harmonics and non-harmonic signals [12], we expect to detect a difference in the relative contribution from the two modes to the total cantilever amplitude in the sample-free case and in the presence of the tip-sample interaction. Using the receding horizon Kalman filter the corresponding contributions from the two modes are decoupled to provide the respective estimated amplitude for the first mode, $\hat{y}_1$, and second mode, $\hat{y}_2$. For the purpose of comparing the relative contribution of the two modes during different scanning parameters, the ratio of the two modes' RMS amplitudes are compared. In addition, it is important to note that each mode constitutes the resonant frequency of that mode and the surrounding frequencies are influenced by that mode. The actual deflection in nanometers is only available for the signal at the first and second mode resonant frequencies from the inverse optical lever sensitivity values. Even though the second mode RMS amplitude was larger when the tip was in tapping contact with the samples, the deflection of the cantilever at the second mode resonant frequency is less due to the smaller second mode inverse optical lever sensitivity.

Figure 4.2 and Figure 4.3 show the topography image of the PLMA-PBMA and mica imaged using bimodal AFM. The large size PLMA, intermediate size PLMA, and PBMA domains [32] are marked in red in Figure 4.2. Let *r* denote the ratio of the second mode RMS amplitude to the first mode RMS amplitude, the ratio of the amplitude contribution for three tip-sample interaction levels are shown in Table 4.2. Approximately 0.5 second of data was used to calculate the RMS of $\hat{y}_1$ and $\hat{y}_2$. The sample-free amplitude was acquired to establish a baseline for the first mode and second mode contribution.

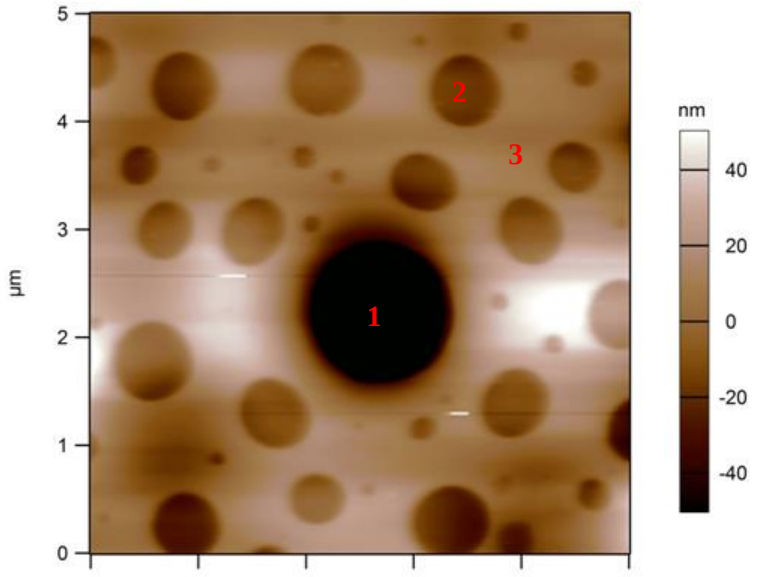

Figure 4.2: Topography of the spin-coated PLMA/PBMA sample taken with bimodal excitation. Force curves were taken at the three regions marked in red. Regions 1, 2, and 3 are the larger size PLMA domain, intermediate size PLMA domain, and PBMA, respectively. The artificial horizontal stripes in the image are due to image flattening in the AFM software.

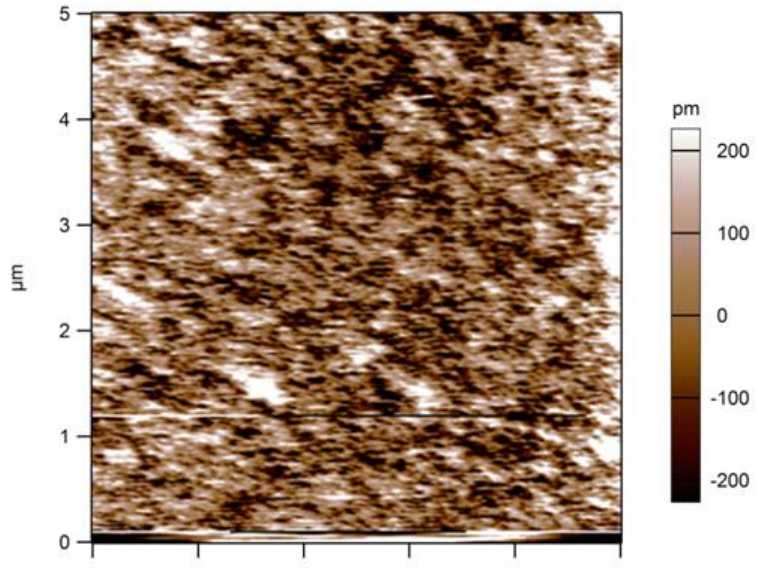

Figure 4.3: Topography image of mica

	A/A_o	$\hat{y}_1$ RMS (V)	$\hat{y}_2$ RMS (V)	r	$\hat{y}_1$ RMS % Change	$\hat{y}_2$ RMS % Change
Sample-free	1	0.2366	0.2097	0.886	0	0
Tip scanning Mica	0.75	0.1659	0.1896	1.143	-29.9	-9.6
Tip scanning PLMA-PBMA	0.7	0.1544	0.1856	1.202	-34.7	-11.5

Table 4.2: RMS values of the estimated amplitude for the two modes. A and A_o are the setpoint amplitude and cantilever free air amplitude, respectively.

To further investigate the contribution of the second mode with increasing tip-sample interaction force, a series of amplitude versus Z sensor force curves were taken on mica and on the PLMA-PBMA domains. The Z sensor is a linear variable differential transformer used to track the distance traveled by the nonlinear Z piezo that moves the cantilever in the vertical direction. The receding horizon Kalman filter was used to decompose the measured amplitude into the estimated first and second mode amplitude. A sliding RMS algorithm with a window of 1000 points was used to calculate the RMS of each mode's amplitude signal. The resulting first mode and second mode RMS versus Z sensor force curves are plotted in Figure 4.4 and Figure 4.5. The first mode RMS values for mica and PBMA domain show rapid initial decrease in amplitude that is characteristic of harder samples. Mica has a larger elastic Young's modulus compared to the polymer sample. For the polymer sample, the PBMA domain is glassy with a Young's modulus of approximately 2GPa, and is thus stiffer at room temperature whereas the PLMA domains are rubbery and softer with Young's modules in MPa range [17]. The softer PLMA domains show a more gradual initial decrease in amplitude. The second mode RMS values show two interesting trends. First, there is an initial increase in the RMS amplitude for mica and the PBMA domain before the RMS amplitude decreases with increasing tip-sample interactions. Second, the final RMS amplitude values for mica and PBMA are larger than those of the PLMA domains. Furthermore, the large size PLMA domain has smaller second mode RMS amplitude compared to the intermediate size PLMA domain. The observation that the larger PLMA domains are softer was also noted in another experiment in the real time mapping of stiffness and dissipative forces of PLMA-PBMA [6].

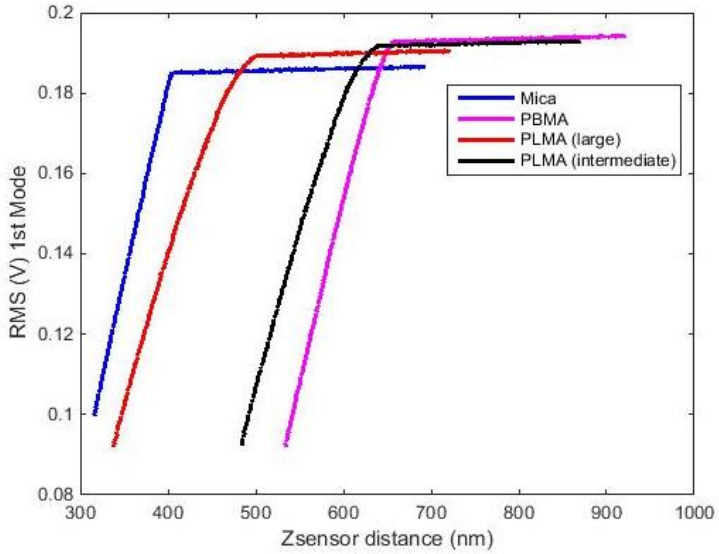

Figure 4.4: Estimated first mode RMS amplitude vs. Zsensor

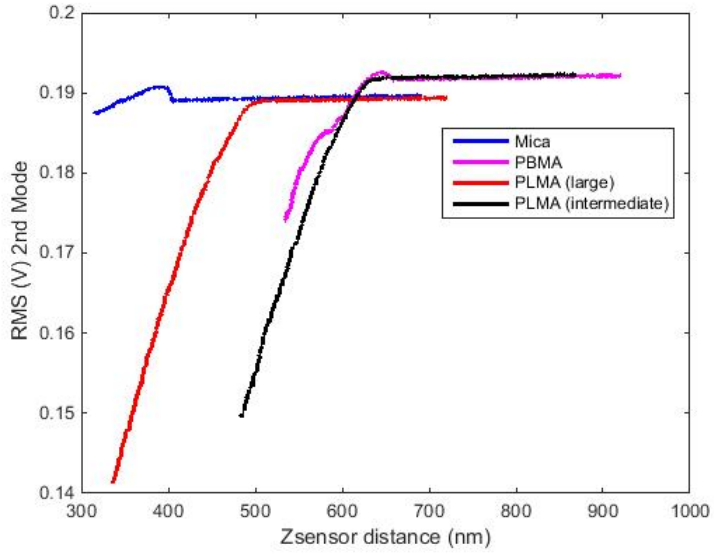

Figure 4.5: Estimated second mode RMS amplitude vs. Zsensor

In Figure 4.6 the ratio of the RMS of $\hat{y}_2$ to $\hat{y}_1$ was plotted as a function of the Z sensor distance for the above force curves. The data show the follow trend:

$$r_{\text{mica}} > r_{\text{PBMA}} > r_{\text{PLMA (intermediate)}} > r_{\text{PLMA (large)}}$$

The result agrees with the second mode force curves result on the relative stiffness of the samples. Overall, the second mode contribution provides an increase in material stiffness contrast compared to the first mode contribution.

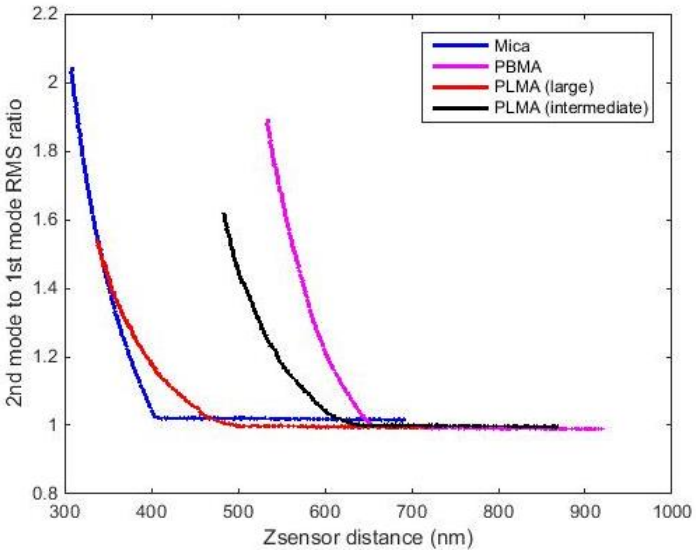

Figure 4.6: Ratio of the Two Modes' RMS Amplitudes vs. Z sensor

4.2 Bimodal Imaging at Varying Input Energy Ratio

This section presents the results of varying the excitation energy of the second mode relative to the energy of the first mode on the PLMA-PBMA sample. The tip was in scanning contact with the PLMA and PBMA domains at 62.5% of cantilever's free amplitude using the first mode's oscillation amplitude as the feedback signal to the AFM's controller. The closed loop XY scanner of the MFP-3D provided a convenient means to image the individual large size PLMA, intermediate size PLMA, and PBMA domains. Four locations of each of type of polymer domains were imaged at each energy level. Using the same frequency response characterization method as discussed in the previous section, the modal parameter of the AC240TS cantilever is shown in Table 4.3.

	1st Mode	2nd Mode
Resonant Frequency *f*	77.55 KHz	450.475 KHz
Quality Factor *Q*	242.098	381.69
Inverse Optical Lever Sensitivity	85.92 nm/V	67.73 nm/V
Spring Constant *k*	2.18 N/m	53.35 N/m

Table 4.3: Modal parameters of the first and second eigenmodes

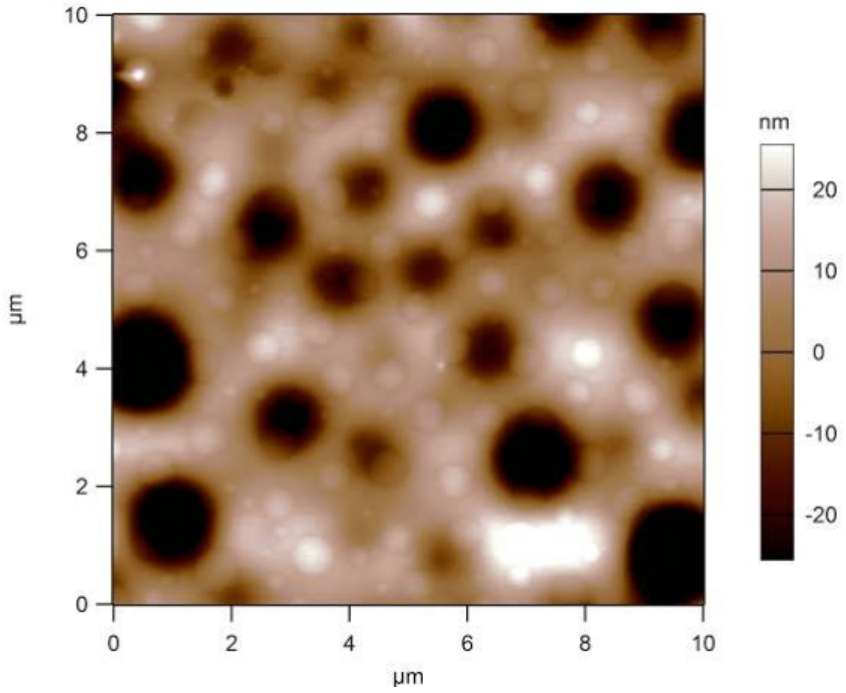

Figure 4.7: Topography of the spin-coated PLMA/PBMA sample taken with bimodal excitation. The large PLMA domains appeared as 'valleys'.

The receding horizon Kalman filter decouples the first and second modes' contribution from the measured cantilever deflection. The function *bandpower* in Matlab calculates the sum of the square of the signal and divides it by the signal length. This function quantifies the average power of the estimated modal deflection $\hat{y}_1$ and $\hat{y}_2$ over a defined frequency range by using a modified power spectra density estimate to compute the average power in that frequency range. The average power of various frequency ranges were calculated and compared at E2:E1 input energy levels equal to 0.03:1, 0.2:1, 1:1, 5:1, and 30:1. Figure 4.8 and Figure 4.9 show the first and second modes' average bandpower, respectively, in the range from 1 KHz to 75 KHz under different E2:E1 ratios for the three polymer regions: large size PLMA, intermediate size PLMA, and PBMA. The selected frequency range excludes the first mode resonant frequency (77.55 KHz) and is far away from the second mode resonant frequency (450.475 KHz). The 1:1 input energy data in Figure 4.8 shows clear statistical average power difference of the large size PLMA domain from the intermediate size PLMA and PBMA domains. However, average power values of the intermediate size PLMA and PBMA domains overlap. On the other hand, the second mode contribution of the same 1:1 energy ratio dataset in Figure 4.9 shows that the three polymer

domains are distinguishable well within their standard deviations. A different trend is seen in the 0.03:1 energy input ratio dataset. The PBMA domains in that dataset have statistically lower average power than that of the PLMA domains. All other energy level ratio datasets in Figure 4.8 and Figure 4.9 show no statistical difference among the three polymer domain types.

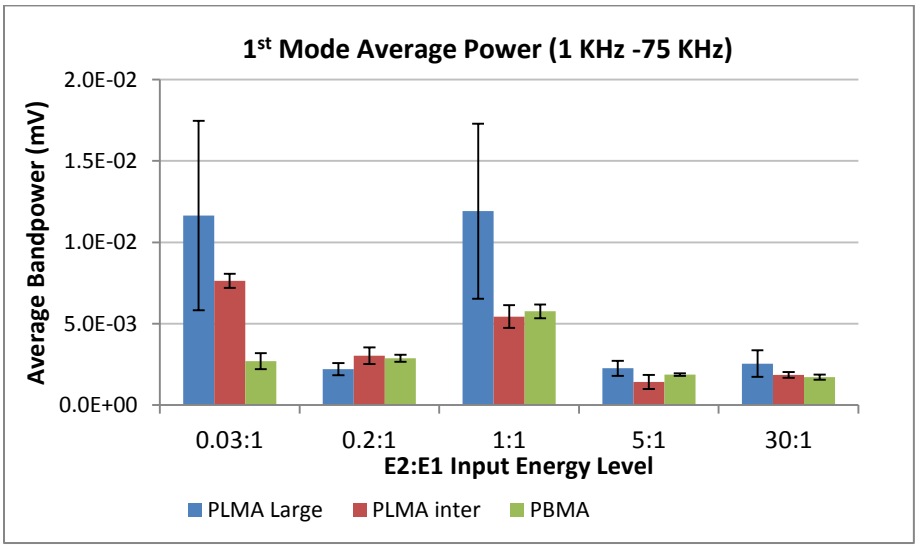

Figure 4.8: First mode average bandpower on 1 KHz to 75 KHz frequency range

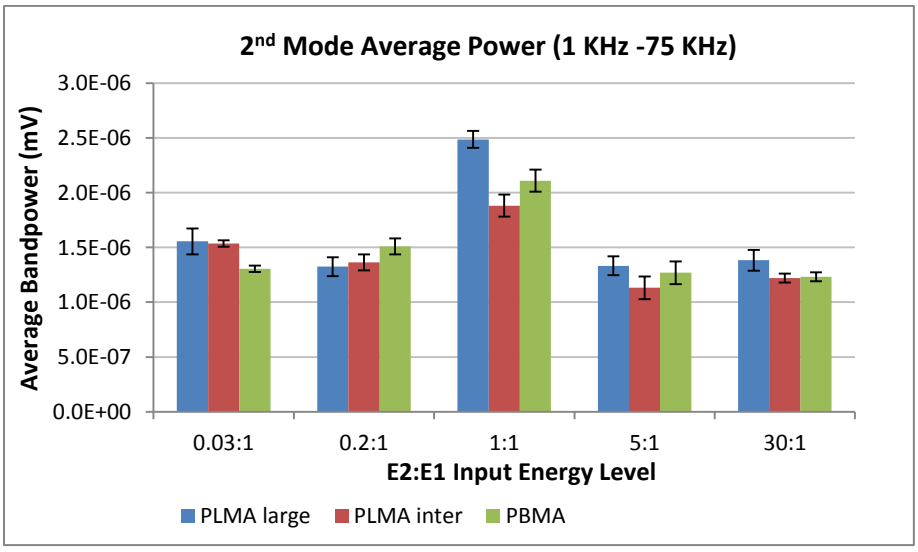

Figure 4.9: Second mode average bandpower on 1 KHz to 75 KHz frequency range

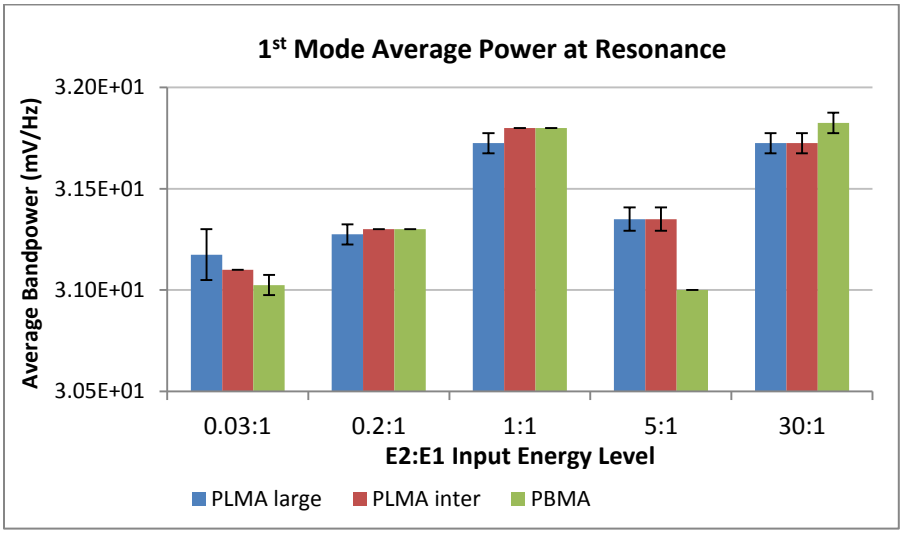

Figure 4.10: Average bandpower of the first mode at resonance frequency

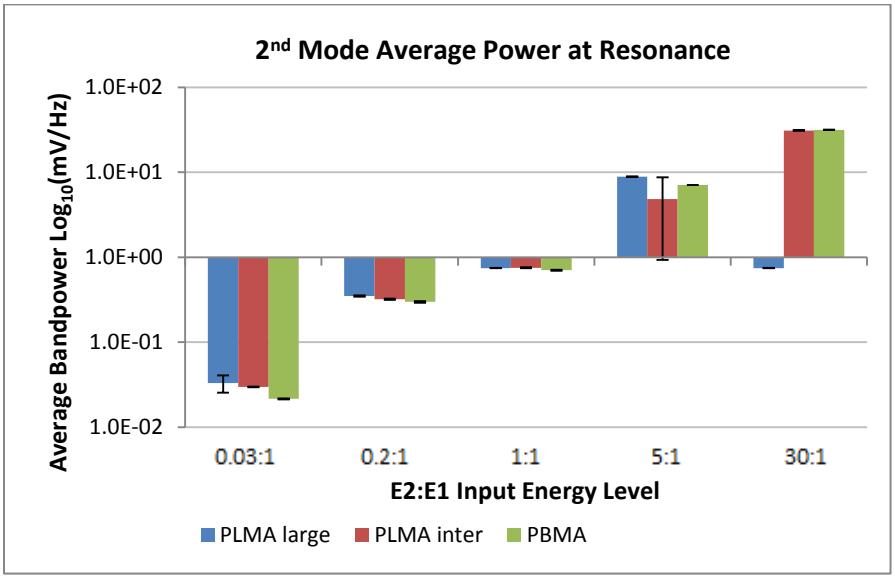

Figure 4.11: Average logarithm of the bandpower of the second mode at resonance frequency

One hypothesis that this experiment tries to address is whether quantifying the average power of the decoupled deflection frequencies away from the modal resonances provides a method to differentiate the three types of polymer. It is thus of interest to compare the average bandpower values of the three polymer domains at the modal resonance frequencies. Figure 4.10 and Figure 4.11 show the average bandpower of the demodulated first and second eigenmodes at

the different input energy ratios. Upon inspection the two graphs do not show that the average power at resonance could distinguish one polymer domain from the others with statistical significance with the exception of the large size PLMA in the 30:1 energy dataset in Figure 4.11 and the PBMA average power in the 5:1 energy dataset in Figure 4.10. Unlike the 1:1 and 0.03:1 energy ratio datasets in Figure 4.8 and Figure 4.9 where the average bandpower values of polymer domains show a consistent trend, the average power values at resonance do not provide a statistically sound method to discern the different polymer types.

In summary, the material property contrast for the three polymer domains is detectable on frequency range away from resonance, and that contrast is dependent on the two modes' relative input energy. These results highlight the potential application of using the receding horizon Kalman filter algorithm and subsequent average power processing to distinguish different polymer domains. The data further indicates that different eigenmode input energy ratio influences the material response in a manner that is not obvious to explain without deeper understanding of eigenmode coupling and frequency-dependence material properties, such as viscoelasticity and creep, of different polymer samples; nevertheless, the results show that imaging parameters such as energy input ratio could be tuned to increase material property contrasts.

Chapter 5: Higher Eigenmode in Liquid

This chapter presents the results and data analysis for liquid imaging using magnetic actuation. Since, in liquid, a soft cantilever's second mode participation is appreciable, as verified by the captured frequency response data during experiments, the drive signal was only applied at the first modal resonant frequency of the magnetic cantilever. Biological applications necessitate the use of cantilever with smaller spring constant and smaller qualify factors; there is approximately a three-fold decrease in quality factor of the cantilever by hydrodynamic damping of the surrounding liquid medium. The higher order fitting and second order curve-fitting of the experimental cantilever frequency response are presented and analyzed. Once the off-sample transfer function for the individual mode was obtained, the state space representation for each mode's model was combined to form a system model for the cantilever in liquid. The receding horizon Kalman filter was applied offline to quantify the first and second modes' contribution in liquid imaging of mica.

The magnetic cantilever used has a spring constant of 0.32 N/m and an inverse optical lever sensitivity 45.01 nm/V in liquid for the first mode. The frequency response of the cantilever far from the sample can be identified using input-output frequency sweep method. The magnitude and phase of the frequency response of a magnetic cantilever immersed in distilled water at distance far away from the mica surface is shown in Figure 5.1. The frequency response shows two poles at 11 KHz and 90 KHz, and a zero at approximately 21 KHz. The blue curve in the phase figure is recorded by the network analyzer, and the red curve is the calculated unwrapped phase.

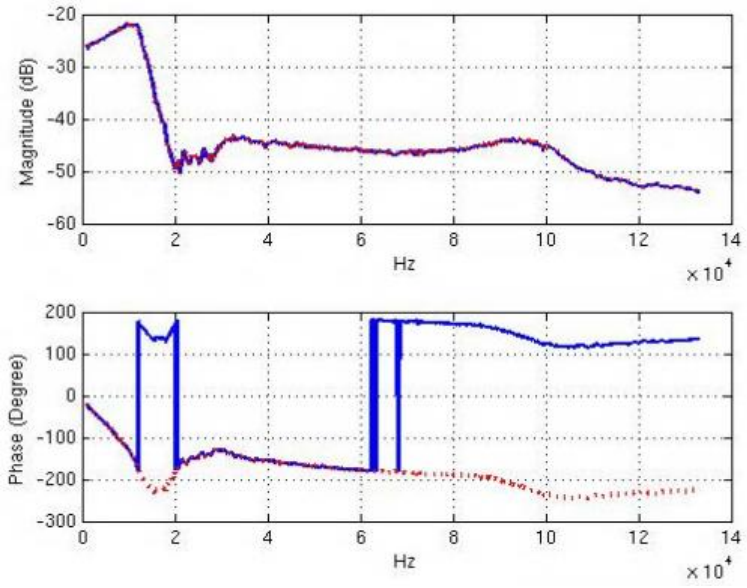

Figure 5.1: Frequency response of the magnetic cantilever in distilled water

The experimental frequency response shows noticeable second mode excitation even when the excitation frequency was close to the first natural frequency. The 180 degrees phase shift at 11 KHz and 90 KHz are due the poles of a second order system, and the rise in phase at 18 KHz is due to a zero in the system. The zero or antiresonance could be due to the coupling of the two modes of the cantilever as a result of low quality factors. The broadening of the peaks is large enough to create coupling of the two modes. In air, coupling of the two modes is negligible due to the high quality factors. The zero between the two poles has been observed in multimodal excitation of cantilevers [33]. The antiresonance represents a zero in the transfer function, and the zero could be changed by changing sensors, and in the cantilever case, the position of the laser spot [32] [33]. Kiracofe et. al. [13] states that the observed antiresonance results from the first and second eigenmode responses being out of phase.

5.1 Fitting of Transfer Functions to Frequency Response Data

Fitting the experimental frequency response to a model is the first step to understand the individual mode's contribution to the cantilever deflection. Since the performance of the Kalman filter relies on the accuracy of the system model, we must fit the frequency response with two modes to obtain an accurate representation of the overall system. Fitting the frequency response could be achieved in many ways. The *fitmagfrd* function in Matlab was used to obtain a minimum phase state space fit. The *fitmagfrd* function fits frequency response to a minimum phase state

space object by using the log-Chebychev magnitude design. The resulting state space system is an 11th order minimum phase system. The high order systems could be generated due to noise in the data. Even though a curve that fits the data is a solution even if it does not match the expected theoretical model, for practical controller design, it is desirable to reduce the model order. Balanced realization and model reduction using *balreal* and *modred* were used to reduce the order of the transfer function by removing the small gain eigenvalues. The final cantilever transfer function is a 7th order minimum phase system shown in Figure 5.2.

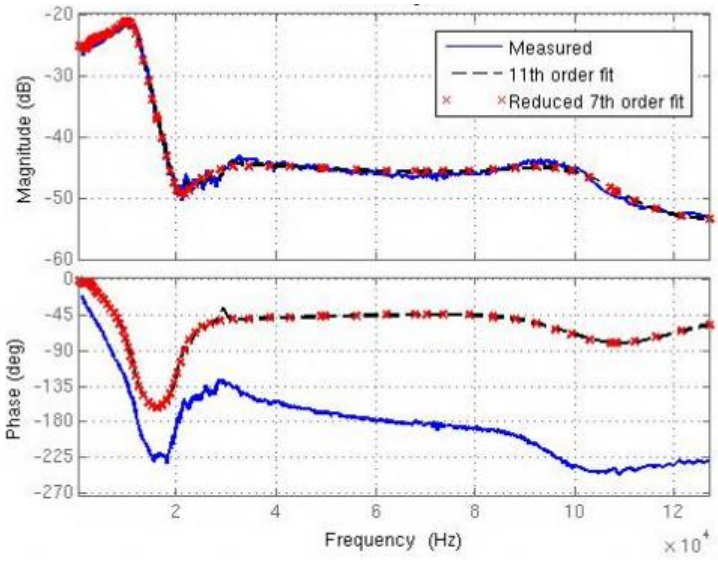

Figure 5.2: Reduced 7th order system

The reduced 7th order system has poles and zeros located at imaginary angular frequency given in Table 5.1.

	jω	Frequency (KHz)
poles	-1.538×10^4	2.448
	$-(1.328 \pm 9.9756i) \times 10^4$	16.014
	$-(0.2407 \pm 1.1122i) \times 10^4$	1.811
	$-(0.0465 \pm 0.2308i) \times 10^4$	0.333
zeros	-1.0139×10^4	16.137
	$-(0.1849 \pm 1.1232i) \times 10^5$	18.117
	$-(0.024 \pm 0.2027i) \times 10^5$	3.249
	$-(0.0037 \pm 0.0196i) \times 10^5$	0.317

Table 5.1: Poles and zeros of the 7th order system

The zero at 18.117 KHz contributes to the antiresonance or minimum magnitude in the frequency response. The pole at 16.017 KHz is very close to the zero at 16.137 KHz, so there is expected to be partial pole-zero cancellation that further contributes to the antiresonance.

5.1.1 Frequency Response Fit Using Simple Harmonic Oscillator

In the SHO model the numerator and denominator of the dynamical system are selected and the coefficients are fitted using a least squares numerical fit functions. The Matlab function *invfreqs* fits a numerator and denominator with real polynomial coefficients of desired orders to the experimental frequency response at given frequencies. For a multimodal system in air, each mode of the cantilever is modeled as a harmonic oscillator with the modal resonant frequency and damping. Assuming a linear interaction, the total response of the cantilever's frequency response is the superposition of the individual eigenmode responses.

The first and second eigenmodes were fitted separately to a simple harmonic oscillator model as shown in Figure 5.3 and Figure 5.4. Because of the low quality factors of the cantilever in liquid and the coupling between the first and second modes, fitting the two modes separately using the ideal SHO model with the first order numerator polynomial and second order denominator polynomial shows large discrepancy. The coupling between the modes skews the expected symmetrical mode shape. In the experimental frequency response of the first mode in Figure 5.3, the total phase shift is 180 degrees until it is near the antiresonance frequency. At approximately 18 KHz the phase then increases, which indicates a zero next to the first pole.

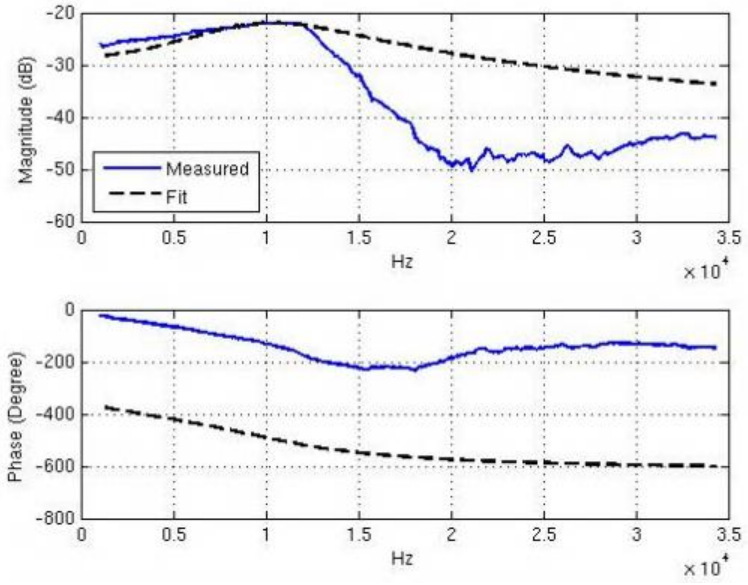

Figure 5.3: Simple harmonic oscillator fit to the first mode

The resonant frequency and qualify factor calculated for the SHO model are 11.1 KHz and 1.119, respectively. The resulting first mode transfer function is

$$\frac{-4104s + 1.842 \times 10^8}{s^2 + 6.235 \times 10^4 s + 4.864 \times 10^9}.$$

	jω	Frequency (KHz)
poles	-(3.1176 ± 6.239i) x 10^4	11.1
zeros	4.488 x 10^4	7.14

Table 5.2: Poles and zeros of the SHO fit for the first mode

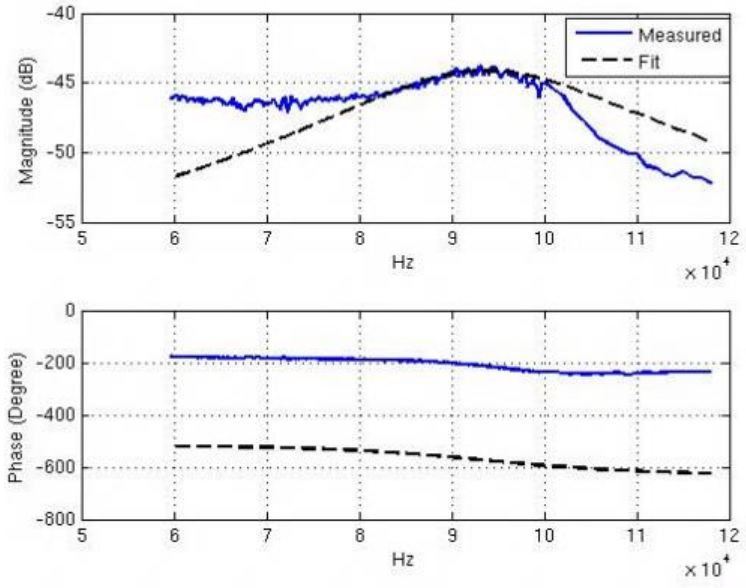

Figure 5.4: Simple harmonic oscillator fit to the second mode

The resonant frequency and qualify factor for the second eigenmode are 94.684 KHz and 2.992, respectively. The corresponding transfer function for the model in Figure 5.4 is

$$\frac{-972.3s-4.5\times10^{8}}{s^{2}+1.988\times10^{5}+3.539\times10^{11}}.$$

	jω	Frequency (KHz)
poles	-(0.9942 ± 5.8655i) x 10^5	94.684
zeros	-4.6285 x 10^5	73.665

Table 5.3: Poles and zeros of the SHO fit for the second mode

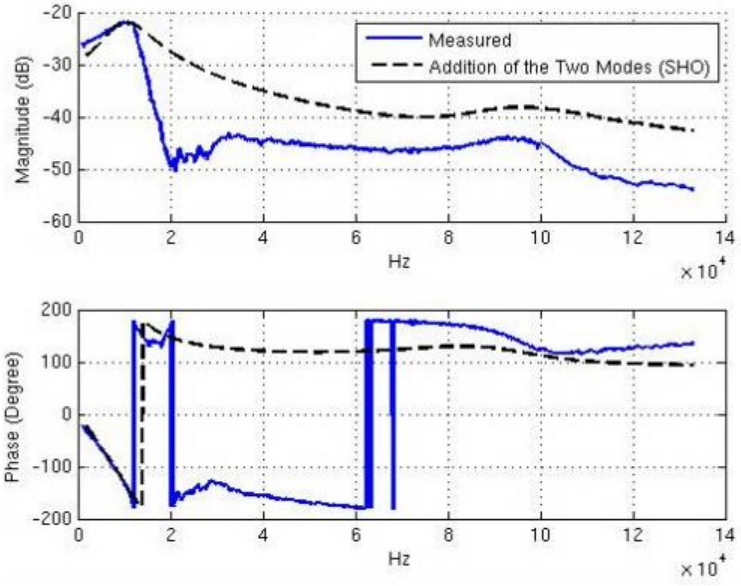

Figure 5.5: Addition of the two modes from the simple harmonic oscillator fit

The transfer function of the sum of the two modes in Figure 5.5 is

$$\frac{-5077s^3 - 1.143 \times 10^9 s^2 - 1.449 \times 10^{15} s + 6.3 \times 10^{19}}{s^4 + 2.612 \times 10^5 s^3 + 3.712 \times 10^{11} s^2 + 2.304 \times 10^{16} s + 1.722 \times 10^{21}}.$$

	jω	Frequency (KHz)
poles	-(0.9942 ± 5.8655i) x 10^5	94.684
	-(3.1176 ± 6.239i) x 10^4	11.1
zeros	0.4185 x 10^5	66.606
	-(1.3345 ± 5.2796i) x 10^5	21.239

Table 5.4: Poles and zeros of the sum of the two modes (SHO fit)

5.1.2 Higher Order Fit to Frequency Response

In Figure 5.6 and Figure 5.7 each mode was separately fitted using *fitfrd*. The *fitfrd* function fits a frequency response data with a state space object. Even though the transfer functions are not guaranteed to be minimum phase, the fit is the best for the lowest possible order.

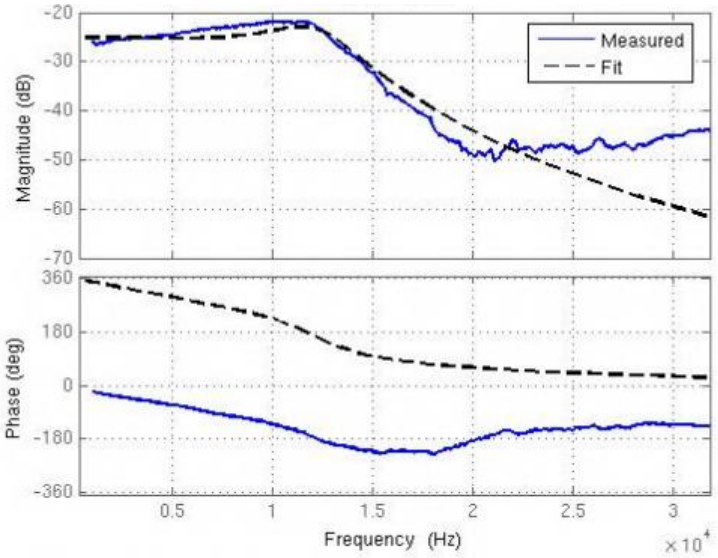

Figure 5.6: Frequency response fit of the first mode using *fitfrd*

The transfer function for the first mode and the locations of the poles and zeros are given below.

$$\frac{-3.382 \times 10^{-7}\, s^3 - 0.05781 s^2 - 1.298 \times 10^{12} s + 1.173 \times 10^{18}}{s^4 + 1.341 \times 10^5 s^3 + 1.236 \times 10^{10} s^2 + 7.399 \times 10^{14} s + 2.103 \times 10^{19}}$$

	jω	Frequency (KHz)
poles	-(1.3223 ± 7.6402i) x 10^4	12.341
	-(5.3842 ± 2.4459i) x 10^4	9.419
zeros	-(0.0005 ± 1.9587i) x 10^9	3.117x10^5
	9 x 10^5	143.24

Table 5.5: Poles and zeros of the first mode using *fitfrd* function

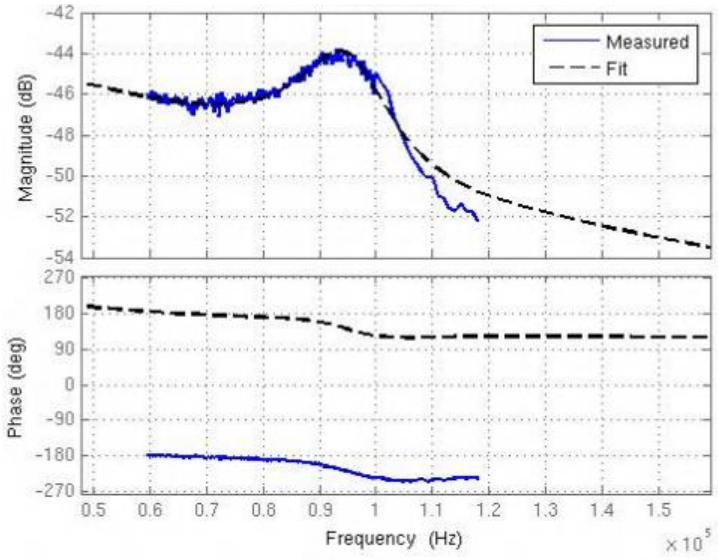

Figure 5.7: Frequency response fit to the second mode using *fitfrd*

The corresponding transfer function for the second mode is

$$\frac{-2252s^3 - 3.77 \times 10^7 s^2 - 7.897 \times 10^{14} s + 1.359 \times 10^{20}}{s^4 + 5.944 \times 10^5 s^3 + 4.561 \times 10^{11} s^2 + 1.846 \times 10^{17} s + 1.842 \times 10^{22}}.$$

	jω	Frequency (KHz)
poles	-(0.4623 ± 5.9681i) x 10^5	95.268
	-1.4335 x 10^5	22.815
	-3.5861 x 10^5	57.075
zeros	1.593 x 10^5	25.353
	-(0.8802 ± 6.0906i) x 10^5	97.942

Table 5.6: Poles and zeros of the second mode using *fitfrd*

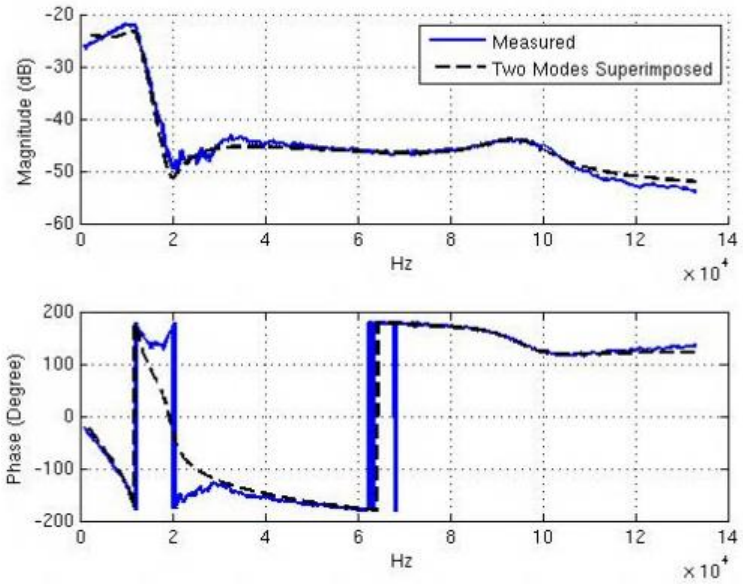

Figure 5.8: Superposition of the two modes

Figure 5.8 shows the sum of the two modes. The poles and zeros of the resulting 8th order transfer function are given below. The right half plane zero could be changed with moving the laser dot along different part of the cantilever [32]. For controller design, the plant zeros could be fitted to remove the right half plane zeros since the RHP zeros place fundamental limits on the speed of the system's response [34].

	jω	Frequency (KHz)
poles	$-(0.4623 \pm 5.9681i) \times 10^5$	94.985
	-3.5861×10^5	57.075
	-1.4335×10^5	22.815
	$-(0.1322 \pm 0.764i) \times 10^5$	12.34
	$-(0.5384 \pm 0.2446i) \times 10^5$	94.118
zeros	$-(0.8814 \pm 6.0906i) \times 10^5$	97.954
	1.8532×10^5	29.495
	$(0.1141 \pm 1.2208i) \times 10^5$	19.514
	$-(0.9137 \pm 0.4409i) \times 10^5$	16.147

Table 5.7: Poles and zeros of the sum of two mode using *fitfrd*

5.1.3 Localized Frequency Response Fit

Localized fitting of each individual mode was also performed using the *fitmagfrd* function. Weights were selected for the localized fitting. Each mode is a second order minimum phase system.

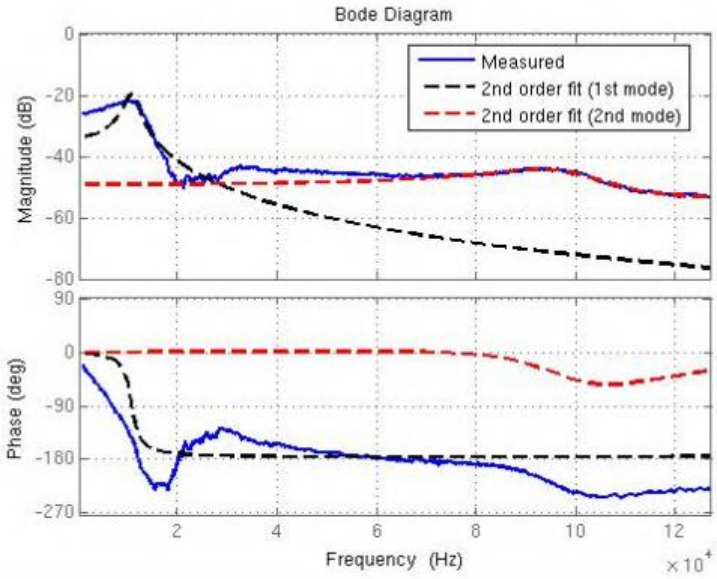

Figure 5.9: Localized fit with weights using *fitmagfrd*

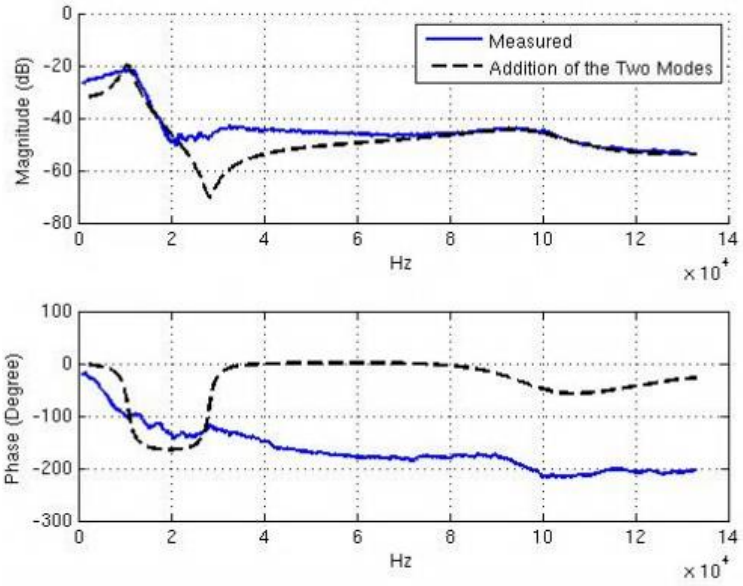

Figure 5.10: Sum of the two modes using *fitmagfrd*

The resonant frequency and quality factor for the first mode are 10.761 KHz and 4.8444, respectively. The first mode transfer function is

$$\frac{7.591s + 9.559 \times 10^7}{s^2 + 1.396 \times 10^4 s + 4.571 \times 10^9}.$$

	jω	Frequency (KHz)
poles	-(0.6978 ± 6.725i) x 10^4	10.761
zeros	-12596 x 10^7	2.00 x 10^7

Table 5.8: Poles and zeros of the first mode using *fitmagfrd* function

The resonant frequency and quality factor for the second mode are 97.39 KHz and 4.3258, respectively. The second mode transfer function is

$$\frac{0.002604s^2 + 633.2s + 1.294 \times 10^9}{s^2 + 1.415 \times 10^5 + 3.744 \times 10^{11}}.$$

	jω	Frequency (KHz)
poles	-(0.7073 ± 6.0782i) x 10^5	97.39
zeros	-(1.2159 ± 6.9444i) x 10^5	112.2

Table 5.9: Poles and zeros of the second mode using *fitmagfrd* function

Figure 5.10 shows the superposition of the two modes from the localized fit. The location of the antiresonance relies more heavily on the accuracy of the first mode fit. The left half plane complex zeros are located at 28.281 KHz and 113.370 KHz. The left half plane complex poles are located at 10.761 KHz and 97.390 KHz. The zero at 28.281 KHz coincides with the antiresonance in the combined response in Figure 5.10.

Overall, fitting an experimental data, such as the frequency response data in Figure 5.1, to a reasonable order system model requires applying valid system dynamics approximation without compromising on the model fidelity. Various fitting functions in Matlab were explored to generate a cantilever state space model, and the corresponding zeros and poles of each model were presented. Although the second order SHO model is a good approximation for the individual cantilever mode in air, Section 5.1.1 shows that the SHO model cannot capture the more complex cantilever dynamics observed liquid, such as antiresonance between the first and second modes due to modal energy coupling. In addition, even though the 7th order, minimum

phase system presented in Section 5.1 provides the best curve fit to the entire measured frequency response data, that model is not suitable for the RHKF algorithm since the two modes are coupled during the fitting. Furthermore, the localized fitting of the experimental data presented in Section 5.1.3 shows good fitting of the second mode but not the first mode; consequently, the linear superposition of these two modes produced a frequency response, shown in Figure 5.10, that deviates from the measured data. Among the different models generated, the combined 8^{th} order system presented in Section 5.1.2 captures the observed antiresonance and provides the necessary decoupled state space models for the RHKF algorithm.

5.2 Modal Contribution of the Measured Deflection

The receding horizon Kalman filter takes the cantilever plant model, voltage input to the solenoid, and cantilever oscillation amplitude from the photodiode to generate an estimate of the cantilever amplitude for each mode. The cantilever model used was the 8^{th} order system that shows the best fit to the experimental frequency response. The Kalman observer was initialized with zero initial states and an error covariance with diagonal covariance entries equaled to 10. The process noise covariance entries for the first mode and second mode were set to 10 and 100, respectively, since the second mode was excited through thermal noise. The measurement noise matrix with covariance values of 1 was used.

Figure 5.11 shows the power spectral density and time domain plots of the excitation signal and measured cantilever deflection. The time domain signal shows the motion of the cantilever in tapping contact with mica in water. The cantilever in Figure 5.11(d) was driven near its fundamental frequency at 11.72 KHz at 78% of its free oscillation amplitude. As shown in Figure 5.11(c), the second mode resonates the most with the 8^{th} and 9^{th} harmonics of the drive frequency.

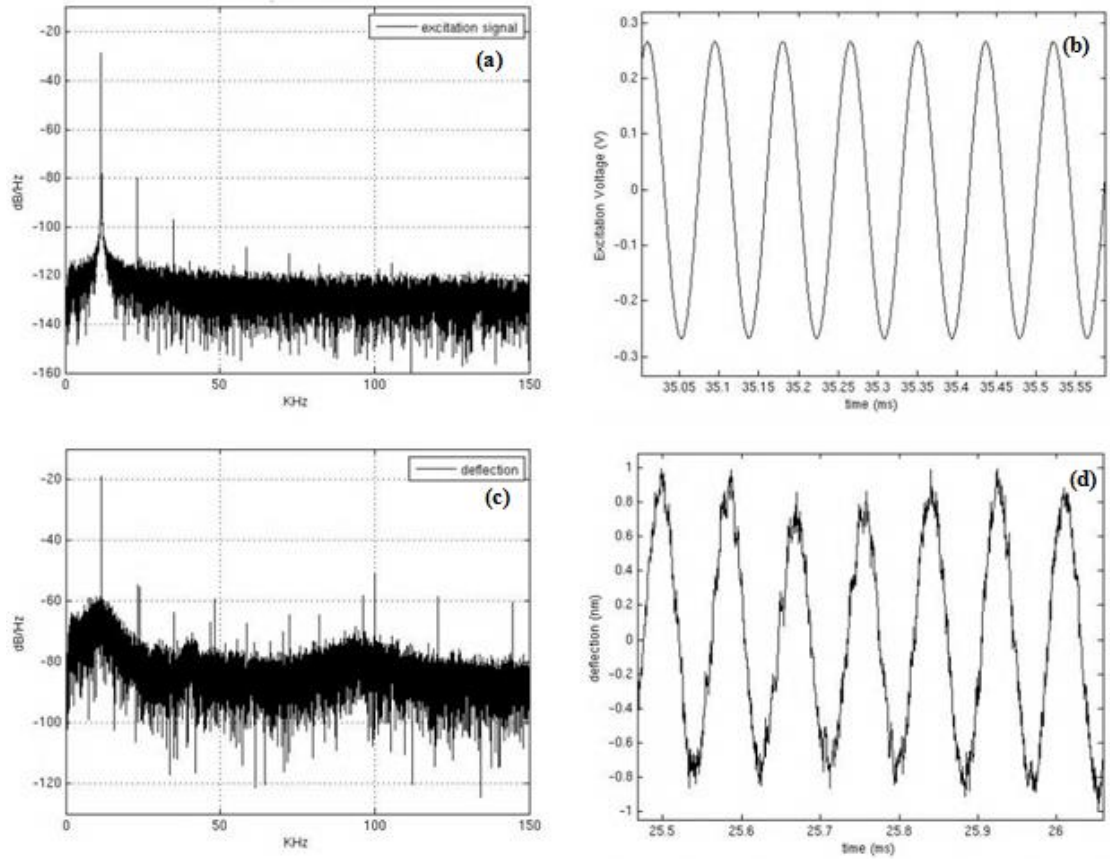

Figure 5.11: (a) and (b) shows the power spectral density and time domain of the excitation signal, respectively. (c) and (d) shows the power spectral density and time domain of the measured cantilever deflection, respectively.

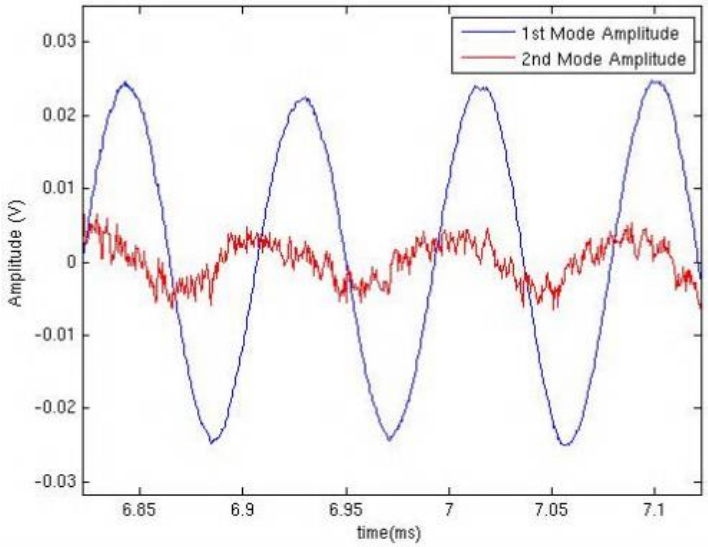

Figure 5.12: Estimated first mode and second mode oscillation amplitude. Since the second mode inverse optical sensitivity was not measured, the y-axis is expressed in volts to allow qualitative comparison of the two modes' estimated sample-free oscillation.

A/A_o	$\hat{y}_1$ RMS (V)	$\hat{y}_2$ RMS (V)	r	$\hat{y}_1$ RMS % Change	$\hat{y}_2$ RMS % Change
1 (Sample-free)	0.0178	0.0056	0.315	0	0
0.78	0.0145	0.005	0.345	-18.5	-10.7
0.65	0.012	0.0051	0.425	-32.6	-8.9
0.52	0.0099	0.0054	0.545	-44.4	-3.6

Table 5.10: RMS of the estimated individual mode amplitude in liquid

The cantilever amplitude and excitation signals for the one sample-free case and the three scanning-amplitude-setpoint cases were acquired. The receding horizon Kalman filter was used to estimate the first mode and second mode cantilever amplitude using the state space model where each mode was a 4^{th} order fit. Figure 5.12 shows the oscillation amplitude of the first and second modes. The amplitude in volts was used since the second mode's photodiode sensitivity was not directly measured. Table 5.10 shows the RMS of the individual modes and the ratio of the second mode RMS to the first mode RMS at different level of tip-sample interaction. Similar to the bimodal experiment in air in Section 4.1, the sample-free case in liquid has the largest RMS second mode contribution. The first mode shows decreased cantilever amplitude with increasing tip-sample interaction since the first mode amplitude was used as the feedback signal. In the presence of the sample, there is a small but detectable increase in the estimated second mode

RMS as the tip-sample interaction increased. A force curve of the sample might be able to provide more data points for how the second mode contribution changes as the tip varies the force exerted onto the sample.

One of the challenges in this experiment is to maintain sufficient cantilever oscillation amplitude using the magnetic actuator in liquid imaging. The existing solenoid actuator used has good magnetic torque capacity in air; however, with the additional hydrodynamic damping in liquid, the torque exerted on the cantilever significantly decreased. A better magnetic actuator that could provide more torque to the cantilever will allow more force to be exerted onto the sample to see the larger effect of the second mode. A robust magnetic actuator's characteristics include uniform magnetic field, irrespective of whether the tip is perpendicular to the sample surface, high bandwidth and magnetic torque without driving large amount of current through the solenoid to avoid large wire inductance, and no appreciable decrease in torque as the tip-sample distance varies.

In conclusion, AFM imaging in liquid presents more complexity as compared to operation in air or vacuum. First, the spurious peaks in the frequency sweep data using acoustic actuation makes it difficult to obtain a valid cantilever model. This is addressed by using a solenoid-based magnetic actuator to drive a soft cantilever in liquid. Second, the participation of higher mode in liquid suggests that a single mode approximation becomes insufficient. Indeed, the experimental data show noticeable second mode participation even though the cantilever was excited only at its first flexure mode, indicating the presence of some energy transfer between adjacent modes in liquid. Furthermore, the data suggest that in the presence of the sample, the participation of the second mode became larger as the tip tapped harder on the sample. Overall, this chapter provides preliminary results of the second mode participation in liquid and demonstrates the usefulness of a state estimation framework to capture and quantify this higher mode participation.

Chapter 6: Microtubules Imaging In Liquid

AFM is a prevalent imaging tool in the study of cells, proteins, and molecular interactions [35]. Other widely used microscopy techniques in biology are the transmission electron microscope (TEM) and fluorescence microscopy. In TEM, a thin specimen is irradiated with a beam of electrons to obtain sub-nanometer lateral resolution. The main drawbacks of TEM include laborious sample preparation and the inability to image live samples. Fluorescence microscopy allowed localized imaging of in-vitro live cells that are stained with fluorophore. Although light diffraction places a fundamental limit on the resolution of conventional fluorescence microscopy, the implementation of various techniques used to improve the spatial resolution of fluorescence microscopy is discussed in [36]. AFM, on the other hand, could study biological samples with pico-newton force in their near native environment [17]. The low force imaging is possible due to the negligible capillary force in liquid. In air the formation of a thin water layer on the sample requires a rigid cantilever to pull the tip away from the attractive capillary force. Since this capillary layer is negligible in liquid, low stiffness cantilevers could be used in biological applications.

6.1 Microtubules

Microtubules play a critical role in cell function of eukaryotic cells from cell division, motor protein transport, and building of cytoskeletons [37]. They are highly organized, hollow cylindrical protein polymers consisting of alpha- and beta-tubulin heterodimers arranged end-to-end to form protofilaments. Microtubules are typically 25nm in width and tens of micrometers in length with walls approximately 8 nm thick. The cross section consists of 13 tubulin units. Microtubules have plus and minus ends. The growth and shortening of the plus end is much more rapid compare to that of the minus end during dynamics instability [38]. Figure 6.1 illustrates the polymerization of microtubules. Figure 6.2 shows a high resolution TEM image of microtubules.

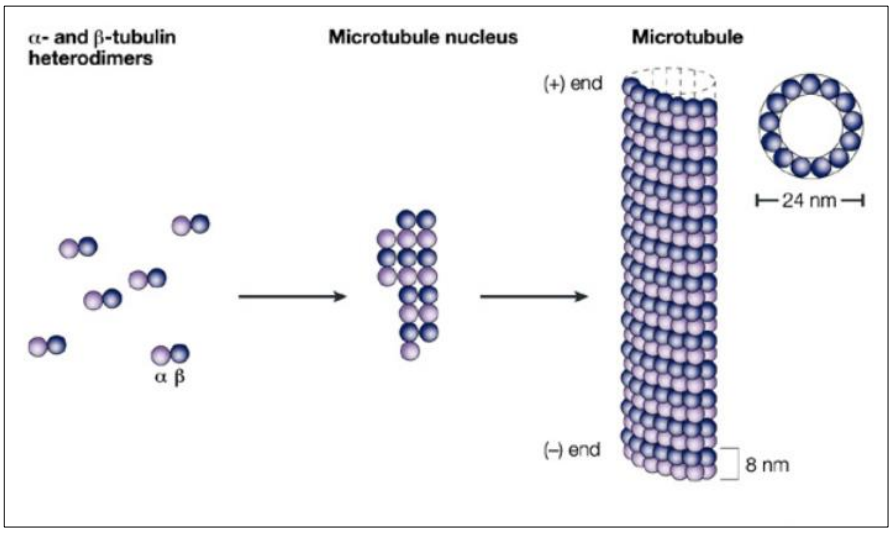

Figure 6.1: Illustration of the microtubule polymerization. The typical microtubule consists of 13 protofilaments. The tubulin heterodimers are arranged in head-to-tail in the 13 protofilaments, with the alpha-tubulin facing the minus end, and the beta-tubulin facing the plus end **[38]**.

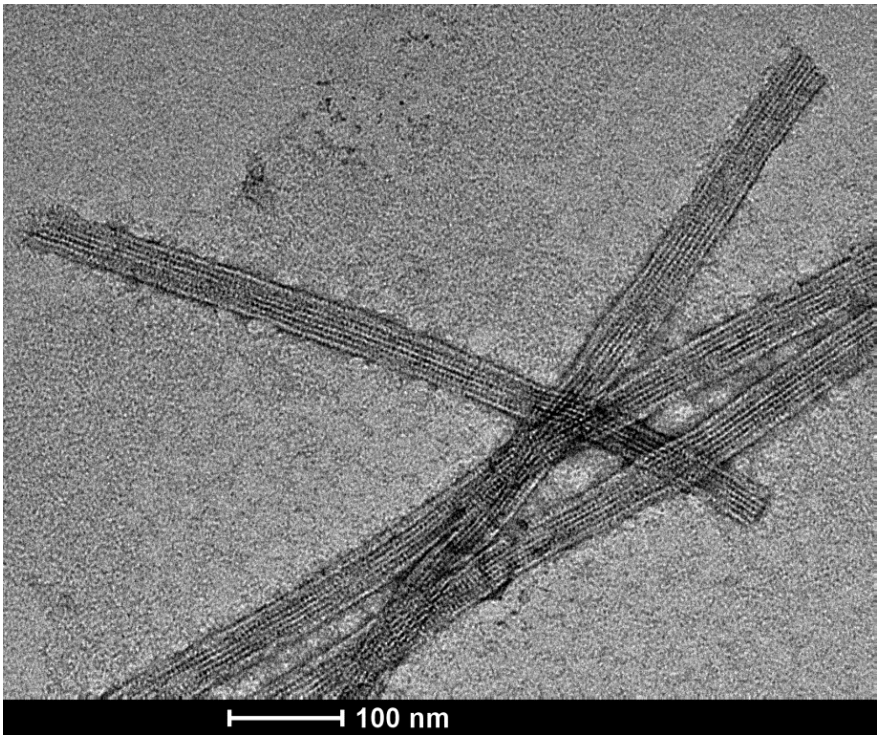

Figure 6.2: TEM image of multiple microtubules. Approximately 7 striations of protofilaments are visible for each microtubule. The width of the microtubule strand is approximately 50nm. The microtubule width is highly dependent on the sample preparation techniques (TEM image provided by Professor M. Gardner's research group at UMN)

6.1.1 Interaction with Motor Proteins

Motor proteins such as kinesin and dynein use energy in the hydrolysis of adenosine triphosphate (ATP) to transport cellular cargos along microtubules [39]. The active movement of kinesin and dynein support important cellular functions such as cell division and axonal transport. Kinesin moves toward the positive ends of microtubules, whereas the dynein moves toward the negative end. Defect in the motor function of kinesin and dynein may lead to various human diseases. As a result, the study of the movement and coordination of these two motor proteins along the microtubule track is a significant multidisciplinary research interest.

Optical tweezer is a single-molecule imaging technique that allows the interrogation of motor proteins with femto-newton force and nanometer spatial resolution. Roychowdhury et. al. [40] designed an active force clamp with force regulation using modern control scheme to probe

motor proteins close to their native cellular environment. The model-based estimation control paradigm allows real time estimation of motor step at higher speed capabilities than previously reported. The description of a kinesin carrying a trapped bead as it walks along the microtubule is described in Figure 6.3.

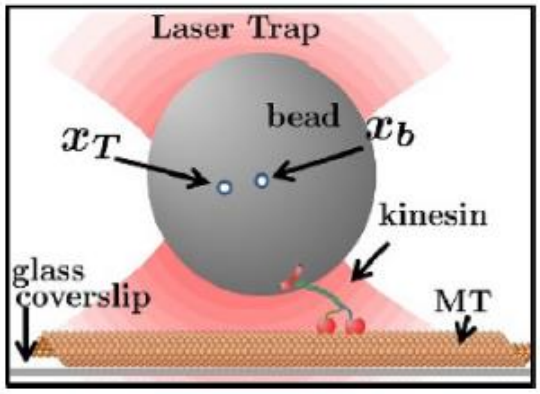

Figure 6.3: The polystyrene bead (cargo) is optically trapped by a laser. The kinesin protein carries the bead and walks along the microtubule that is adhered to a glass substrate. $\boldsymbol{x_t}$ is the trap position, and the bead position $\boldsymbol{x_b}$ changes in response to the force exerted by kinesin and the trap position **[40]**.

6.1.2 Microtubules Tip Structure

Microtubules are in a constant state of polymerization and depolymerization known as dynamic instability [37]. The microtubule grows and shrinks as tubulins attached and detached from the microtubule ends. Microtubule ends undergo an initial slow growth period, and then undergo rapid shortening process known as "catastrophe". The study of the evolution of microtubules' tip structure has provided insights on the dynamic instability of microtubules [41]. Using 3-D mechanochemical simulation, fluorescence microscopy, and electron microscopy techniques, Coombes et. al. [41] reported that evolving structure of the microtubule tip has an active role in the age dependence of the rapid shortening event. The microtubule tip becomes more tapered as it grows, and this destabilizes the tip and leads to catastrophe.

The focus of this chapter is two-fold. First, a sample preparation protocol using physical immobilization is used to adhere microtubules on a flat substrate for AFM imaging in liquid. Second, high resolution AFM images of microtubules are obtained to provide structural insights on microtubules.

6.2 Chemical and Physical Immobilization of Microtubules

One of the main challenges in AFM liquid imaging of biological samples is sample preparation. Chemical and physical adsorption techniques are commonly used for immobilization of biological samples prior to AFM imaging. The biological specimens have to be immobilized on a flat surface, which is usually mica or glass, to differentiate sample and solid substrate. Mica is widely used as an immobilization substrate due to its atomically flat surface. Research groups have used various chemical reagents to treat the mica surface in chemical immobilization [42].

In the physical immobilization process, the net attractive force pulls the specimen onto the solid substrate. This net force involves van der Waals forces, electrostatic double-layer force, and hydration forces. The adsorption process is highly dependent of the buffer pH concentration, ionic strength, and the sample polarity [35]. Weak electrostatic adsorption of the negatively charged microtubules onto the negatively charged muscovite mica is accomplished by adding multivalent cations to the buffer solution.

6.3 Microtubules Adsorption Protocol

Microtubules samples infused with Taxol and BRB80 buffer were provided by Professor M. Gardner's group at the University of Minnesota. Taxol is generally used to stabilize the polymerization of microtubules. The microtubules samples were kept at the incubator set at 37^{o} C when not in use. During sample preparation, an aliquot of the microtubules sample was placed on the freshly cleaved mica. The sample was incubated at 37^{o} C for 2 minutes. The sample was then removed, and an aliquot of BRB80 buffer was added onto the microtubules infused mica before placing the sample in incubator for another 2 minutes. Afterward, the sample was washed gently with BRB80 buffer using a pipette to wash away any disassociated microtubules. The sample was placed under the AFM stage to be imaged. Additional buffer was added to maintain a conical meniscus between the sample and cantilever during imaging.

The microtubules were imaged using the MFP-3D AFM system from Asylum Research. Cantilevers with spring constants of 2.1 N/m (AC240) and 0.08 N/m (TR400PSA) were used. The TR400PSA cantilever has a nominal radius of curvature of 20nm. Spring constants were determined using thermal fluctuation method in the AFM software. In acoustic actuation, the cantilever frequency sweep is dominated by a 'forest of peaks' due to mechanical- or structural-borne vibration of the piezo shake to the surrounding liquid medium. Therefore, selecting the correct resonant frequency for acoustic driven dynamics AFM imaging requires a heuristic

approach. The frequency of the peak to the immediate left of the simple harmonic oscillator fit was chosen as the drive frequency.

6.4 Results and Discussion

This section presents the AFM images of microtubules on mica substrate imaged in buffer. The cross section analysis of the microtubule dimensions is also provided. Figure 6.4 shows the topography of a microtubule strand and the cross section of the microtubule. Figure 6.5 shows amplitude image of the same microtubule strand to illustrate better contrast of the protofilament striation. Figure 6.6 and Figure 6.9 show the aged microtubules with observable weaker mechanical structure.

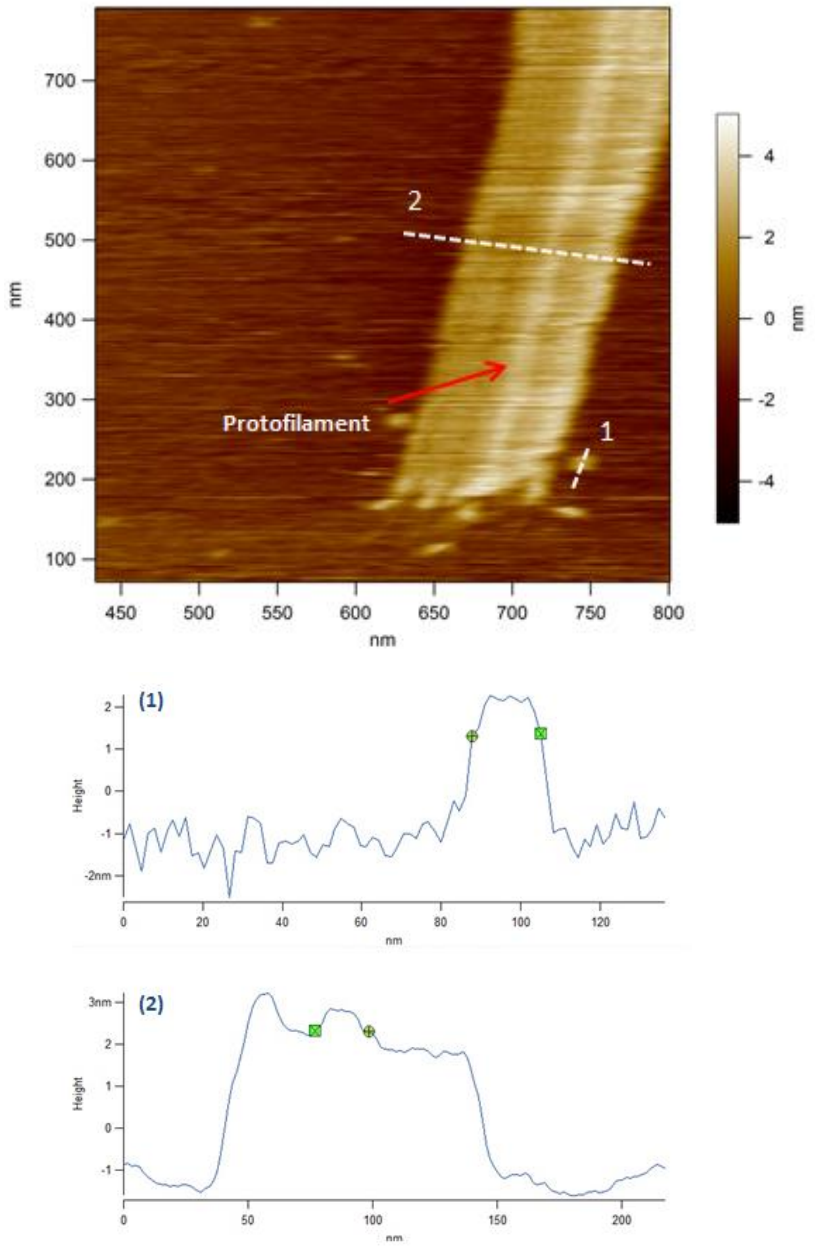

Figure 6.4: The top image shows the topography of a microtubule strand. A soft cantilever with a spring constant of 0.08N/m was used. The outline of a protofilament striation (marked by the red arrow) and dissociated tubulin subunits near the microtubule tip are clearly visible. The cross-section profiles of the microtubules and tubulin unit taken at the dashed lines (1) and (2) are shown below the topography image. A tubulin subunit in (1) has width of 20nm and height of 2.5 nm. The cross section line in (2) shows a similar width of approximately 20nm for the discernable protofilament. The measured width of the microtubule is approximately 110nm. The theoretical width of the microtubule and protofilament is approximately 25nm and 3.5nm, respectively. Due to the large AFM tip radius (~20nm), the tip-sample convolution makes it difficult to distinguish the individual protofilaments and obtain accurate spatial dimension measurements.

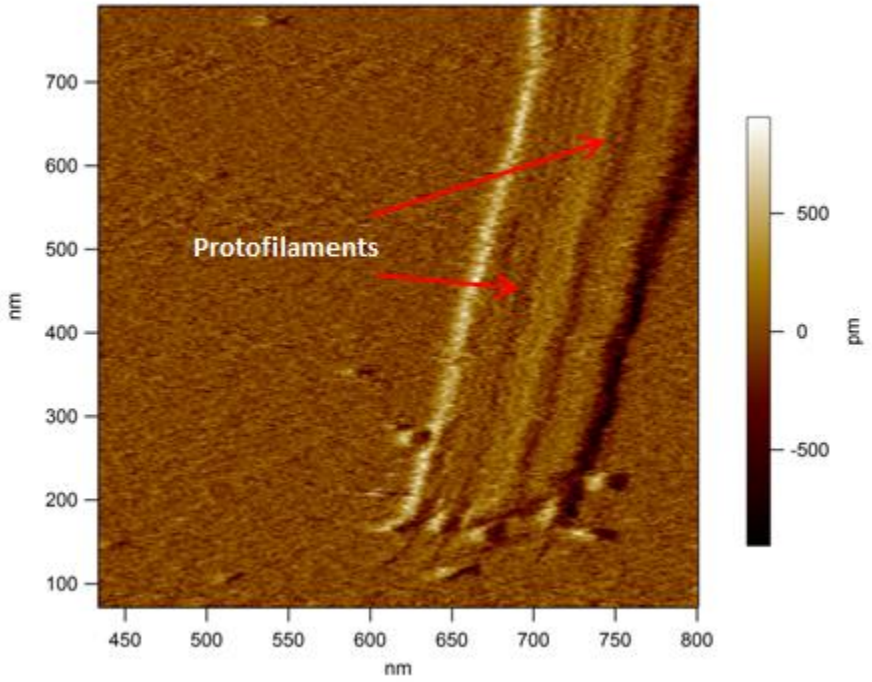

Figure 6.5: Amplitude image of the same microtubule strand shown in Figure 6.4. The protofilaments along the cylindrical axis are marked by the red arrows. The amplitude image shows more contrast of the protofilaments due to the amplitude signal's greater sensitive to sample edge. Loose tubulin subunits are visible next to the jagged microtubules tip.

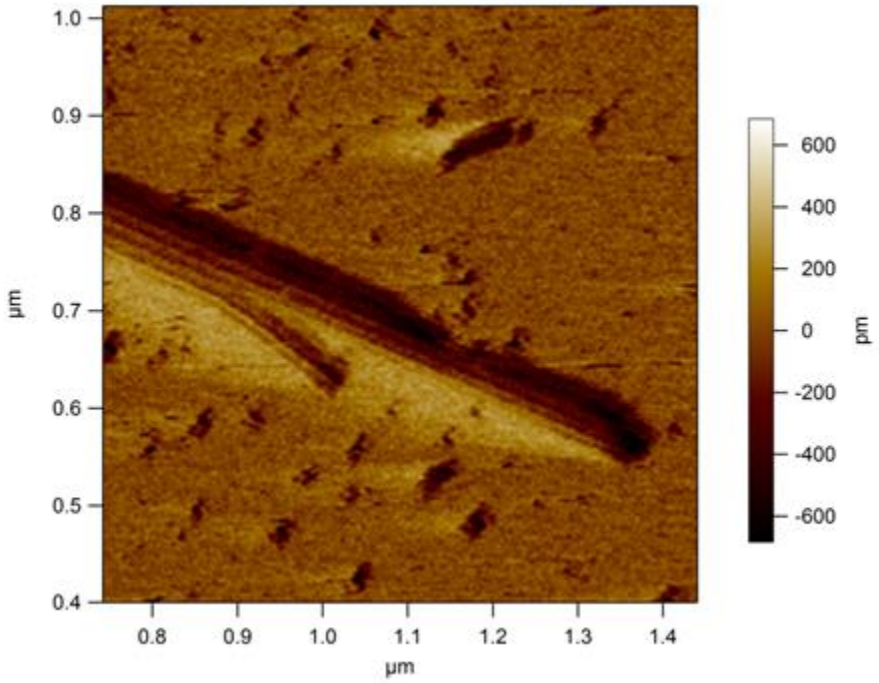

Figure 6.6: Amplitude image a microtubule that has been kept in the incubator at 37^{o}C for 5 days. A soft cantilever was used to reduce the applied force on the microtubule. Six protofilament striations of the partially flattened microtubules are visible. Due to aging, the microtubule structural became more fragile and began to disassemble, as evident by the tapered tip, splitting of the protofilaments, and disassembled tubulin subunits.

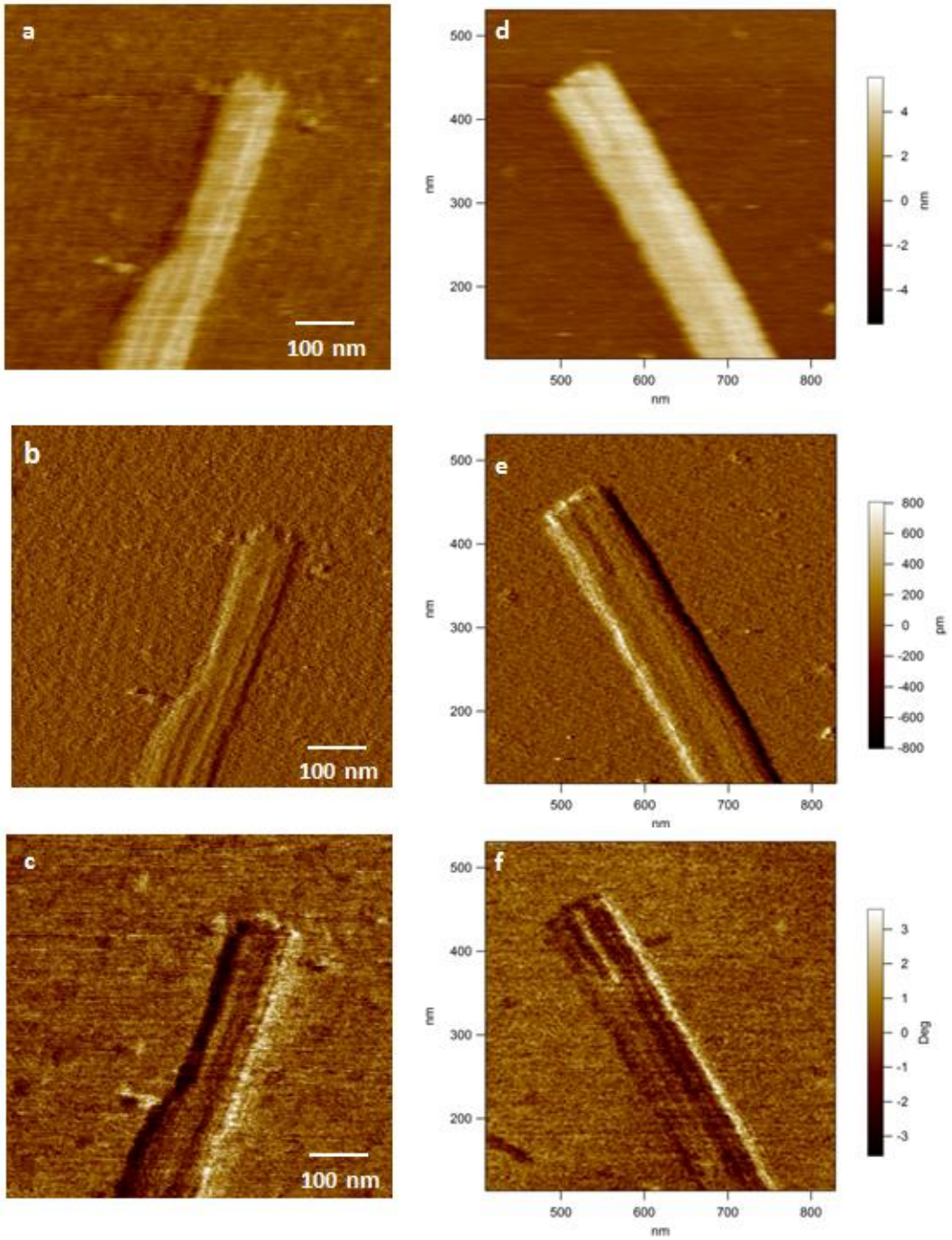

Figure 6.7: Images (a) and (d) show the topography image of two different microtubule strands; the corresponding amplitude images are given in (b) and (f). The corresponding phase images are shown in (c) and (g). These microtubules were imaged using a soft cantilever with a 0.08 N/m spring constant. The three types of image signals provide different level of contrast of the microtubule structure. Two different tip structures are observable. Specifically, the microtubule strand on the left has a jagged, saw-like tip, whereas the microtubule has a blunt tip.

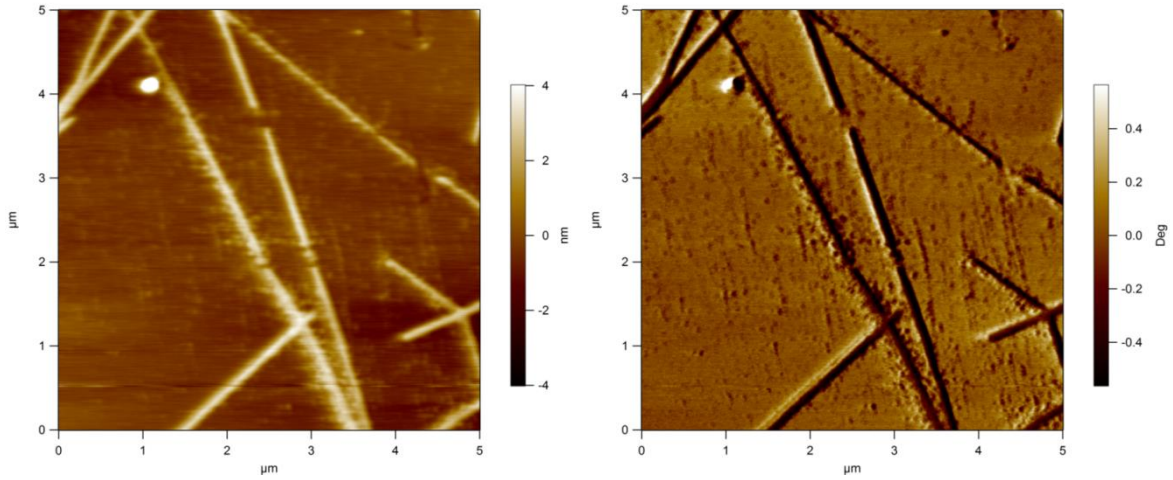

Figure 6.8: 5um x 5um topography (left) and phase (right) image of long microtubules using a stiff cantilever with a nominal spring constant of 2 N/m. The tubulin subunits were scrapped away by the tip as a result of high contact force and repeated scans.

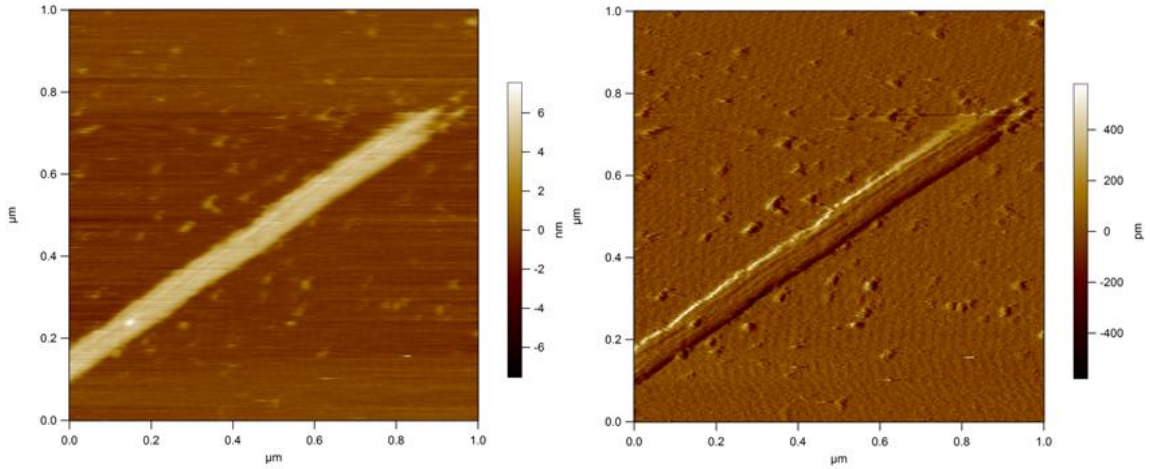

Figure 6.9: Topography and amplitude images of microtubules that were kept in the temperature controlled incubator for 5 days. Disassembled tubulin subunits were scattered in the vicinity of the microtubules. The tip of the aged microtubules is more tapered compared to the young microtubules shown in Figure 6.7. The observation of increasing tapering of tip of aged microtubules is in good agreement with the results presented in **[41]**.

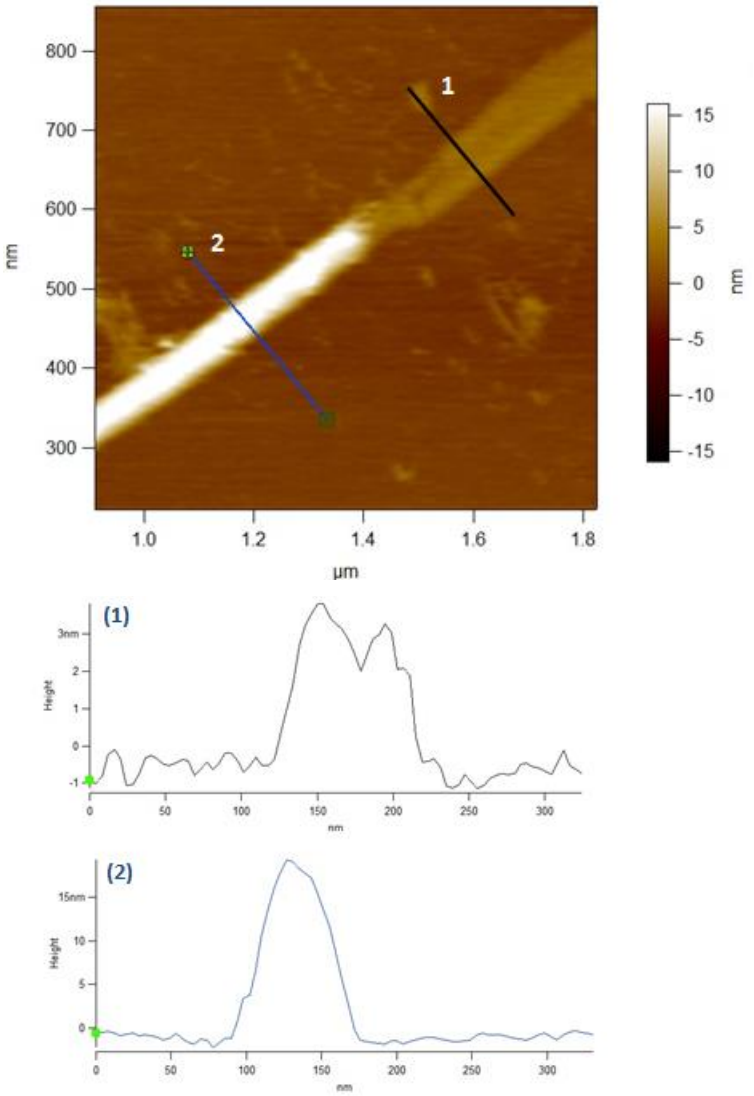

Figure 6.10: Topography (top) and cross-section profiles (bottom) showing the collapsed and non-collapsed regions of the microtubule strand. A collapsed portion and a structurally-intact portion of a microtubule strand are approximately 4 nm and 20 nm tall, respectively. The width of the taller microtubule segment is approximately 100nm, whereas the collapsed segment is wider. The collapse or flattening of the microtubule region might be due to the applied tip force during imaging.

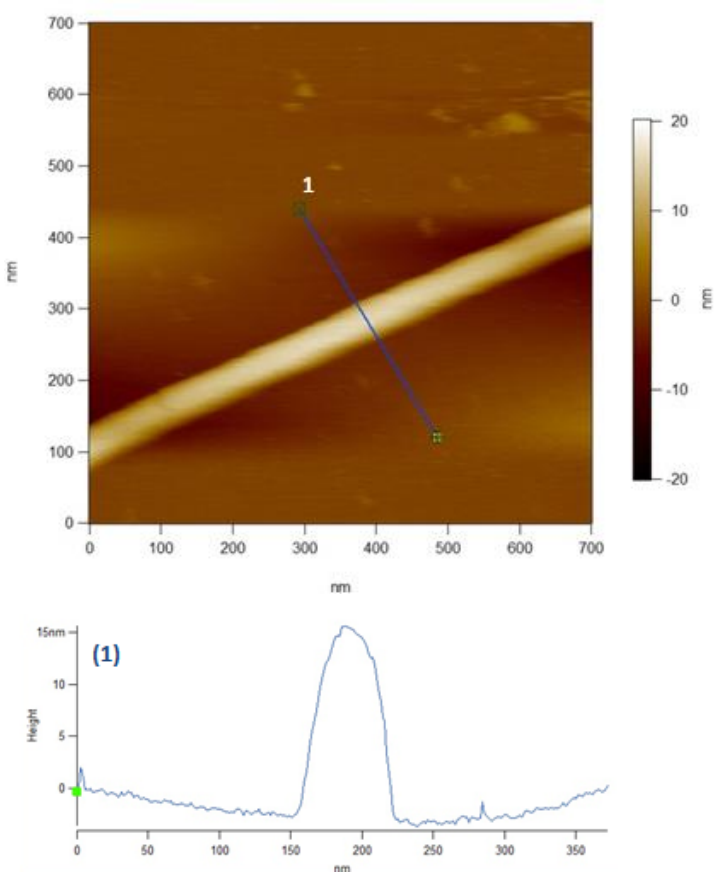

Figure 6.11: The non-collapsed microtubule is 15nm in height. One notable observation is that protofilaments are not visible in the taller microtubule. The width of the microtubule is approximately 75 nm.

In conclusion, this chapter outlines a straight forward sample preparation protocol for microtubules in acoustic liquid imaging that relies on weak electrostatic attraction between microtubules and mica. Stiff and soft cantilevers were used to image the microtubules. Using soft cantilever the protofilaments, loose tubulins, and microtubules with various tip structures are imaged. The measured height of the microtubules is highly dependent on the force exerted by the tip. The average width and height of microtubules are 100 nm and 6 nm, respectively. The broadening of the microtubules could be a result of the collapsing of the microtubule structure, either caused by the tip force or weakened mechanical integrity during the physical immobilization process. Another cause of the apparent broadening of microtubules diameter is the tip-sample convolution. Tip-sample convolution occurs when the AFM probe with a radius of curvature scans over an object with comparable or smaller lateral dimension. The results show

that with the appropriate selection of cantilever and imaging parameter, AFM provides a valuable tool to image and study live cells and proteins in their near native environment.

Chapter 7: Conclusion

The bimodal AFM experiments in air and liquid show the feasibility of using the system approach scheme to quantify the contribution of the first and second eigenmodes, and that additional contrast in material stiffness can be captured with the additional second mode excitation. Provided that the experimental model of the cantilever system, excitation signals, and cantilever amplitude signals are available, this scheme provides the best estimate of each mode's contribution during various levels of tip-sample interaction. For low quality factor systems such as soft cantilevers in liquid imaging, the energy contents of the first two modes of the cantilever are coupled. Unlink the conventional lock-in method, the receding horizon Kalman filter could be used to quantify this eigenmode energy coupling.

One assumption used in this thesis is that the cantilever plant from the sample-free model is valid in the presence of the tip-sample interaction. In large amplitude oscillation in air, the tip travels tens of nanometers and only encounters the repulsive regime of the sample in the last few nanometers of its downward and upward swings. Therefore, each tap on the sample could be modeled as a dirac delta function, and the cantilever plant resets to its sample-free parameters during the rest of the oscillation trajectory [12]. A more rigorous parameter estimation technique such as REEP could be implemented to obtain the equivalent model of the individual modes in the cantilever system at various tip-sample interactions.

Last, the microtubules imaging in buffer provides a protocol that could be adapted for bimodal imaging in liquid using magnetic actuation to provide mapping of material contrast.

Appendix: Receding Horizon Kalman Filter

The discrete Kalman filter provides the optimal state estimation for a discrete linear dynamical system. It is optimal in the least squares sense by minimizing the mean square errors of $x_k - \hat{x}_k$, where $\hat{x}_k$ is the estimate of the state x_k that we wish to estimate based on the available measurements. The Kalman filter uses all k measurements and state estimates to recursively determine the optimal state estimate at time $k+1$. The receding horizon Kalman filter, on the other hand, recursively calculates the optimal state estimate at $k+1$ using the optimal state estimate at time $k-M$ and the most recent $M+1$ output measurement. In this thesis, M is chosen to be 10 photodiode measurements to balance the effect of noise and responsiveness to transients. The selection of M is based on a previous experiments reported by Saraswat et. al. [12].

A.1 AFM Model

The discrete, linear, time-invariant dynamical model for an *N* mode cantilever is described by

$$x(k+1) = Fx(k) + G^L\big(g(k) + \Phi(p,\dot{p})\big) + G\eta(k), \tag{A.1}$$
$$y(k) = Hx(k) + \upsilon(k),$$

where

$$x(k) := [x_1(k)\ x_2(k)\ \ldots\ x_N(k)]',\ F := \begin{bmatrix} F1 & \ldots & 0 \\ 0 & \ddots & 0 \\ 0 & 0 & F_N \end{bmatrix},\ G^L := \begin{bmatrix} G_1^L \\ \vdots \\ G_N^L \end{bmatrix}, \tag{A.2}$$

$$G := \begin{bmatrix} G_1 & \ldots & 0 \\ 0 & \ddots & 0 \\ 0 & 0 & G_N \end{bmatrix},\ \eta(k) := \begin{bmatrix} \eta_1(k) \\ \vdots \\ \eta_N(k) \end{bmatrix}, \text{ and } H := [H_1 \quad \ldots \quad H_N].$$

The dither input, tip-sample interaction forces, process noise, cantilever deflection, and measurement noise are denoted by g, $\Phi(p,\dot{p})$, η, y, and ν, respectively. F, G^L, G, and H are characterized from the frequency sweep data. In dynamic mode AFM, the process noise and measurement noise are characterized by the cantilever thermal noise and photodiode detector noise, respectively. They are assumed to be independent of each other and have Gaussian distributions. The process covariance matrix, $S = E(\eta\eta^*)$, and the measurement covariance matrix , $R = E(\nu\nu^*)$, are assumed to be constant.

A.2 Receding Horizon Kalman Filter Dynamics and Implementation

The RHKF dynamics is described by the following:

$$\hat{x}_{k+1} = F\hat{x}_k + FP_kH^T(HP_kH^T + R)^{-1}[y_k - \hat{y}_k] + G^L g_k\,, \tag{A.3}$$
$$\hat{y}_k = H\hat{x}_k\,,$$
$$P_{k+1} = F[I - P_kH^T(HP_kH^T + R)^{-1}H]P_kF^T + GSG^T.$$

At each time k, the dynamics is initialized at the $(k-M)^{th}$ instance. The implementation of the RHKF is an iterative process and is composed of an a priori time update, or prediction step, and an a posteriori measurement, or correction step. The time update equations project the state and error covariance ahead in time. The time update equations are

$$\hat{x}_k = F\hat{x}_{k-1} + G^l g_{k-1}\,, \tag{A.4}$$
$$P_k^- = FP_{k-1}F^T + S\,.$$

In the measurement update, the new Kalman gain L_k is computed. This Kalman gain is then used to update the estimate with measurement y_k and the error covariance P_k. The measurement update equations are

$$L_k = P_k^-H^T(HP_k^-H^T + R)^{-1}, \tag{A.5}$$
$$\hat{x}_k = \hat{x}_k^- + L_k(y_k - H\hat{x}_k^-)\,,$$
$$P_k = (I - L_kH)P_k^-.$$

The initial estimates for $\hat{x}_{rh}(k-M) = 0$ and $P_{k-M} = P_0$ are used at each iteration.

A.3 Matlab Code

The Matlab function *recedingHorizonKF* is used to implement the RHKF filter. A parallel *for* loop was used to increase the computation efficiency. The following are input parameters to the function.

def: deflection output voltage
dither: excitation input voltage
list: past M measurements used in the receding horizon
Q_n: process covariance matrix
R_n: measurement covariance matrix

dA_cmb: F matrix in equation (A.1)

dB_cmb: G^L matrix in equation (A.1)

dC_cmb: observation matrix, H, in equation (A.1)

dD _cmb: feedforward matrix from the experiment model

dC1: observation matrix H_1 of the first mode model

dC2: observation matrix H_2 of the second mode model

dD1: feedforward matrix of the first mode model

dD2: feedforward matrix of the second mode model

```
---------------------------------------------------------------------------
function
[ystack1,ystack2]=recedingHorizonKF(def,dither,list,Q_n,R_n,dA_cmb,dB_cmb,dC_cmb,dG_c
mb,dC1,dC2,dD1,dD2)
clear ystack1 ystack2  % estimated deflection from the 1st and 2nd mode
def1=def;
   ystack1=zeros(length(list),length(def1));
   ystack2=zeros(length(list),length(def1));
N=list;
clear xhat Pn yhat1 yhat2
clear xhat1 xhat2 xhat3 xhat4 xhat_cm
   xhat1=zeros(1,(length(def1)-N));
   xhat2=zeros(1,(length(def1)-N));
   xhat3=zeros(1,(length(def1)-N));
   xhat4=zeros(1,(length(def1)-N));

   Pn=zeros((length(def1)-N),4,4);
   Pn1=10*eye(4);
   Pn2=zeros(length(N),4,4);
   Mn=zeros(length(N),4);
   for j=N:-1:1
      Pn2(N-j+1,:,:)=Pn1;
      Pn3=squeeze(Pn2(N-j+1,:,:));
      Mn(N-j+1,:)=Pn3*dC_cmb'*(dC_cmb*Pn3*dC_cmb'+R_n)^-1; %Measurement Update
      Pn1=Pn1-Mn(N-j+1,:)'*dC_cmb*Pn1;
      Pn1=dA_cmb*Pn1*dA_cmb' + dG_cmb*Q_n*dG_cmb';
   end

parfor k=1:(length(def1)-N)
   i=k+N;
   xhatk=zeros(4,1);
   for j=N:-1:1
      %Measurement Update
      xhatk=xhatk+ Mn(N-j+1,:)'*(def1(i-j)-dC_cmb*xhatk);
      %Time Update
```

```
        xhatk=dA_cmb*xhatk+dB_cmb*dither(i-j);
    end
    xhat1(k)=xhatk(1);
    xhat2(k)=xhatk(2);
    xhat3(k)=xhatk(3);
    xhat4(k)=xhatk(4);
    Pn(k,:,:)=Pn1;
    xhat_cm=[xhat1(k);xhat2(k);xhat3(k);xhat4(k)];

    yhat1(k)=[dC1 0*dC2]*xhat_cm+dD1*dither(i);
    yhat2(k)=[0*dC1 dC2]*xhat_cm+dD2*dither(i);
end
ystack1(p,1:length(yhat1))=yhat1;
ystack2(p,1:length(yhat1))=yhat2;
```

Bibliography

1] G. Binning, C. F. Quate and C. Gerber, "Atomic Force Microscope," *Phys. Rev. Lett,* vol. 56, p. 930, 1986.

2] S. M. Salapaka and M. V. Salapaka, "Scanning Probe Microscopy," *Control Systems Magazine, IEEE,* vol. 28, no. 2, pp. 65-83, 2008.

3] R. Garcia and A. San Paulo, "Attractive and repulsive tip-sample interaction regimes in tapping-mode atomic force microscopy," *Physical Review B,* vol. 60, no. 7, 1999.

4] A. Sebastian, M. Salapaka, D. Chen and J. Cleveland, "Harmonic and power balance tools for tapping-mode atomic force microscope," *Journal of Applied Physics,* vol. 89, p. 6473, 2001.

5] D. Sahoo, A. Sebastian and M. Salapaka, "Transient-signal-based sample-detection in atomic force microscopy," *Applied Physics Letters,* vol. 83, p. 5521, 2003.

6] G. Saraswat, P. Agarwal, G. Haugstad and M. Salapaka, "Real-time probe based quantitative determination of material properties at the nanoscale," *Nanotechnology,* vol. 24, 2013.

7] R. Stark and W. Heckl, "Higher harmonics imaging in tapping-mode atomic-force microscopy," *Review of Scientific Instruments,* vol. 74, p. 5111, 2003.

8] R. Proksch, "Multifrequency, repulsive-mode amplitude-modulated atomic force microscopy," *Applied Physics Letters,* vol. 89, p. 113121, 2006.

9] J. Lozano and R. Garcia, "Theory of Multifrequency Atomic Force Microscopy," *Physical Review Letters,* vol. 100, p. 076102, 2008.

10] S. Basak and A. Raman, "Dynamics of tapping mode atomic force microscopy in liquids: Theory and experiments," *Applied Physics Letters,* vol. 91, p. 064107, 2007.

11] J. Melcher, C. Carrasco, X. Xu, J. Carrascosa, J. Gomez-Herrero, P. de Pablo and A. Raman, "Origins of phase contrast iin the atomic force microscope in liquids," *PNAS,* vol. 106, no. 33, pp. 13655-13660, 2009.

12] G. Saraswat and M. Salapaka, "On contribution and detectin of higher eigenmodes during dynamic atomic force microscopy," *Applied Physics Letters,* vol. 102, p. 173108, 2013.

D. Kiracofe and A. Raman, "Nonlinear dynamics of the atomic force microscope at
13] the liquid-solid interface," *Physical Review B,* vol. 86, p. 205405, 2012.

G. Saraswat, P. Agarwal and M. Salapaka, "Multimode and multitone analysis of the
14] dynamic mode operation of the Atomic Force Microscope," in *American Control Conference (ACC)*, Washington DC, 2013.

M. Salapaka, H. Bergh, J. Lai, A. Majumdar and E. McFarland, "Multi-mode noise
15] analysis of cantilevers for scanning probe microscopy," *Journal of Applied Physics,* vol. 81, p. 2480, 1997.

T. Rodriguez and R. Garcia, "Tip motion in amplitude modulation (tapping-mode)
16] atomic-force microscopy: Comparison between continuous and point-mass models," *Applied Physics Letters,* vol. 80, p. 1646, 2002.

G. Haugstad, Atomic Force Micrscopy: Understanding Basic Modes and Advanced
17] Applications, Hoboken: John Wiley & Sons, Inc, 2012.

D. Sahoo, A. Sebastian and M. Salapaka, "Harnessing the transient signals in atomic
18] force microscopy," *International Journal of Robust and Nonlinear Control,* vol. 15, pp. 805-820, 2005.

D. Sahoo, T. De and M. Salapaka, "Observer based imaging method for Atomic
19] Force Microscopy," in *44th IEEE Conference on Decision and Controls*, Seville, 2005.

J. Cleveland, B. Anczykowski, A. Schmid and V. Elings, "Energy dissipation in
20] tapping-mode atomic force microscopy," *Applied Physics Letters,* vol. 72, no. 20, 1998.

P. Agarwal and M. Salapaka, "Real time estimation of equivalent cantilever
21] parameters in tapping mode atomic force microscopy," *Applied Physics Letters*, vol. 95, p. 083113, 2009.

A. Sebastian, D. Sahoo and M. Salapaka, "An observer based sample detection
22] scheme for atomic force microscopy," in *Proceeding of the 42nd IEEE Conference on Decision and Control*, Maui, 2003.

S. Ghosal and M. Salapaka, "Fidelity imaging for atomic force microscopy," *Applied*
23] *Physics Letters,* vol. 106, p. 013113, 2015.

A. Gelb, Applied Optimal Estimation, Cambridge: M.I.T. Press, 1974.

24]

25] G. Welch and G. Bishop, "An Introduction to the Kalman Filter," University of North Carolina: Chapel Hill, 2006.

26] W. Kwon, P. Kim and P. Park, "A Receding Horizon Kalman FIR Filter for Discrete Time-Invariant Systems," *IEEE Transactions on Automatic Control,* vol. 44, no. 9, 1999.

27] J. Kokavecz and A. Mechler, "Investigation of fluid cell resonances in intermittent contact mode atomic force microscopy," *Applied Physics Letters,* vol. 91, p. 023113, 2007.

28] A. Raman, J. Melcher and R. Tung, "Cantilever dynamics in atomic force microscopy," *Nano Today,* vol. 3, 2008.

29] S. Hoof, N. Gosvami and B. Hoogenboom, "Enhanced quality factors and force sensivity by attracting magnetic beads to cantilevers for atomic force microscopy in liquid," *Journal of Applied Physics,* vol. 112, p. 114324, 2012.

30] G. Jayanth, Y. Jeong and C. Menq, "Direct tip-position control using magnetic actuation for achieving fast scanning in tapping mode atomic force microscopy," *Review of Scientific Insrtruments,* vol. 77, p. 053704, 2006.

31] M. Kageshima, T. Chikamoto, T. Ogawa, Y. Hirata, T. Inoue, Y. Naitoh, Y. Li and Y. Sugawara, "Development of atomic force microscope with wide-band magnetic excitation for study of soft matter dynamics," *Review of Scientific Instruments,* vol. 80, p. 023705, 2009.

32] G. Haugstad and K. Wormuth, "Environmental Digital Pulsed Force Mode and Confocal Raman Microscopy in Biomedical Coatings Research," in *NSTI Nanotech Conference Proceedings,* 2009.

33] F. Rubio-Sierra, R. Vazquez and R. Stark, "Transfer function analysis of the micro cantilever used in atomic force microscopy," *IEEE Transactions on Nanotechnology,* vol. 5, 2006.

34] V. Pini, B. Tiribilli, C. Gambi and M. Vassalli, "Dynamical characterization of vibrating AFM cantilevers forced by photothermal excitation," *Physical Review B,* vol. 81, p. 054302, 2010.

35] S. Skogestad and I. Postlethwaite, Multivariable feedback control: analysis and design, Wiley, 2007.

L. Hamon, P. Curmi and D. Pastre, "Chapter 9 - High-Resolution Imaging of

36] Microtubules and Cytoskeleton Structures by Atomic Force Microscopy," *Methods in Cell Biology,* vol. 95, pp. 157-174, 2010.

37] B. Huang, M. Bates and X. Zhuang, "Super resolution fluorescence microscopy," *Annu Rev Biochem.,* vol. 78, pp. 993-1016, 2009.

38] C. Waterman-Storer, "Microtubules and microscopes: how the development of light microscopic imaging technologies has contributed to discoveries about microtubule dynamics in living cells," *Molecular Biology of the Cell,* vol. 9, pp. 3263-3271, 1998.

39] M. Jordan and L. Wilson, "Microtubules as a target for anticancer drugs," *Nature Reviews Cancer,* vol. 4, pp. 253-265, 2004.

40] A. Gennerich and R. Vale, "Walking the walk: how kinesin and dynein coordinate their steps," *Current Opinion in Cell Biology,* vol. 21, pp. 59-67, 2009.

41] S. Roychowdhury, A. T. and M. Salapaka, "High bandwidth optical force clamp for investigation of molecular motor motion," *Applied Physics Letters,* vol. 103, no. 15, 2013.

42] C. Coombes, A. Yamamoto, M. Kenzie, D. Odde and M. Gardner, "Evolving tip structures can explain age-dependent microtubule catastrophe," *Current Biology,* vol. 23, pp. 1342-1348, 2013.

43] A. Vinckier, I. Heyvaert, A. D'Hoore, T. McKittrick, C. Haesendonck, Y. Engelborghs and L. Hellemans, "Immobilization and imaging microtubules by atomic force microscopy," *Ultramicroscopy,* vol. 57, pp. 337-343, 1995.

44] A. Vinckier, C. Dumortier, Y. Engelborghs and L. Hellemans, "Dynamical and mechanical study of immobilized microtubules with atomic force microscopy," *Journal of Vacuum Science & Technology B,* vol. 14, p. 1427, 1996.

45] D. Muller and Y. Dufrene, "Atomic force microscopy as a multifunctional molecular toolbox in nanobiotechnology," *Nature Nanotechnology,* vol. 3, 2008.

46] D. Kiracofe, A. Raman and D. Yablon, "Multiple regimes of operation in bimodal AFM: understanding the energy of cantilever eigenmode," *Beilstein Journal of Nanotechnology,* pp. 4,385-393, 2013.

47] A. Kis, S. Kasas, B. Babic, A. Kulik, W. Benoit, G. Briggs and C. Schonenberger, "Nanomechanics of Microtubules," *Physical Review Letters,* vol. 89, no. 24, 2002.

R. Vazquez, J. Rubio-Sierra and R. Stark, "Multimodal analysis of force

48] spectroscopy based on a transfer function study of micro-cantilever," *Nanotechnology*, vol. 18, p. 185504, 2007.